

# ToMCCA-3: A realistic 3-body coalescence model

Maximilian Mahlein<sup>1</sup>, Bhawani Singh<sup>1,5</sup>, Michele Viviani<sup>2</sup>,  
Francesca Bellini<sup>3</sup>, Laura Fabbietti<sup>1</sup>, Alejandro Kievsky<sup>3</sup>,  
Laura Elisa Marcucci<sup>4,3</sup>

<sup>1</sup>Technical University of Munich, TUM School of Natural Sciences, Physics Department,  
James-Franck-Straße 1, 85748 Garching b. München, Germany

<sup>2</sup> INFN Pisa, Largo B. Pontecorvo 3, I-56127 Pisa, Italy

<sup>3</sup> Dipartimento di Fisica e Astronomia A. Righi, Università di Bologna  
and INFN Bologna, Via Irnerio 46, 40126 Bologna, Italy

<sup>4</sup> Dipartimento di Fisica. Università di Pisa, Largo B. Pontecorvo 3, I-56127 Pisa,  
Italy and Sezione INFN, Pisa, Italy

<sup>5</sup> Thomas Jefferson National Accelerator Facility, Newport News, VA 23606, USA

April 4, 2025

## Abstract

The formation of light nuclei in high-energy collisions provides valuable insights into the underlying dynamics of the strong interaction and the structure of the particle-emitting source. Understanding this process is crucial not only for nuclear physics but also for astrophysical studies, where the production of rare antinuclei could serve as a probe for new physics. This work presents a three-body coalescence model based on the Wigner function formalism, offering a refined description of light-nucleus production. By incorporating realistic two- and three-body nuclear interaction potentials constrained by modern scattering and femtoscopic correlation data, our approach improves on traditional coalescence models. The framework is validated using event generators applied to proton-proton collisions at  $\sqrt{s} = 13$  TeV to predict the momentum spectra of light (anti) nuclear nuclei with mass number  $A = 3$ , which are then compared with the experimental data from ALICE. Our results demonstrate the sensitivity of light nucleus yields to the choice of nuclear wave functions, emphasizing the importance of an accurate description of the coalescence process. This model lays the foundation for the extension of coalescence studies of  $A = 3$  light nuclei to a wider range of collision systems and energies.

## 1 Introduction

One of the fundamental open questions in nuclear and particle physics, as well as astroparticle physics, is understanding the formation mechanisms of light nuclei and antinuclei—such as deuterons and helium—in high-energy interactions. In recent years, research on antimatter nuclei heavier than antiprotons has seen significant advancements on both experimental and theoretical fronts.

This question has received particular attention at high energy hadron colliders such as the Large Hadron Collider (LHC) and the Relativistic Heavy Ion Collider (RHIC). Due to the large integrated luminosities delivered over the past decade, multi-differential measurements of light nuclei and antinuclei production could be performed with unprecedented precision. New techniques, such as femtoscopy [1, 2] and correlation studies, have provided deeper insights into the production mechanisms of these bound states.

Light (anti-)nuclei yields and particle ratios measured as functions of the final-state charged-particle multiplicity pseudorapidity density (or *multiplicity*) have evidenced the dependence of nucleus production on the size of the particle emitting source [3, 4, 5, 6, 7]. Different particle species, among which nucleons and strange baryons, are observed to be emitted from a common particle source in proton-proton collisions at center of mass energies of  $\sqrt{s} = 13$  TeV [8, 9], whose radius decreases with transverse

momentum<sup>1</sup>. In addition, pion kaon and proton radii are observed to increase with multiplicity from pp to p-Pb (*small systems*) to heavy-ion collisions (*large systems*) [10, 11]. Moreover, proton-proton (p-p), proton-deuteron (p-d), Lambda-deuteron ( $\Lambda$ -d) and three particle correlations (p-p-p and p-p- $\Lambda$ ) studied with femtoscopy have allowed access to the strong interaction between baryons, shedding light on the three-body forces acting in the system of two-and three-nucleons [12].

Among the light nuclei and antinuclei, deuterons have been measured with the highest precision, as a function of multiple variables such as multiplicity, momentum, and rapidity. Models attempting to describe their formation—including statistical hadronization [13, 14, 15] and coalescence [16, 17, 18, 19, 20], a nuclear fusion-like process in high-energy collisions—have been largely successful, despite relying on different underlying principles. In statistical hadronization models (SHM), light nuclei are produced from a hadron gas in thermal equilibrium and according to the laws of quantum statistics and with an appropriate treatment of the quantum number conservation laws depending on the size of the system. SHM predicted abundances depend on the particle mass, spin, temperature and volume of the system. The coalescence approach describes how individual (anti)nucleons merge into (anti)nuclei based on their proximity in momentum and spatial coordinates. However, discrepancies between the measured and predicted observables remain, particularly in the production of heavier systems such as helium, tritium, and hypertriton (a bound state of a neutron, a proton, and a  $\Lambda$  baryon) [7, 21]. The latter confirms to be a key observable for discriminating between thermal and coalescence production [22, 23, 24] due to its broad size ( $\sim 10$  fm) and small energy ( $\sim 150$  keV) that binds the  $\Lambda$  to the deuteron core [25]. The first hypertriton measurement in p-Pb collisions, supports the coalescence model and disfavors the hypothesis of thermal production [21].

While widely used, coalescence models often involve free parameters—such as the coalescence momentum—whose values are not derived from first principles and vary depending on the production environment. Traditional models assume simple momentum-based coalescence, while more advanced quantum-mechanical approaches incorporate nucleon wave functions and the size of the emission source, according to a Wigner function-based formulation [19, 20, 24]. Such an approach also finds application in recent developments based on Monte Carlo methods that allow us to apply coalescence as an afterburner to particle production [26, 27].

One of the most intriguing applications of the research on (anti)nuclei formation mechanisms is the indirect detection of dark matter (DM) through cosmic antinuclei, such as antideuterons and anti-helions. Unlike standard cosmic ray antimatter (e.g., antiprotons), these antinuclei have a significantly suppressed background from astrophysical sources, making them a promising signature of DM annihilation [28, 29, 30, 31, 32, 33]. However, their production mechanisms remain uncertain, and data from particle accelerators become a key input. The tentative measurements of  ${}^{3,4}\overline{\text{He}}$  antinuclei in cosmic rays by the AMS-02 Collaboration have sparked several studies in order to interpret these findings. Although the experimental results have not been published in a peer-reviewed journal yet, the confirmation of even one such antinucleus would challenge the current understanding of cosmology [34, 35].

In this paper, the coalescence model ToMCCA [36] is extended to the  $A = 3$  case. The predictions include not only the nuclei  ${}^3\text{He}$  and  ${}^3\text{H}$ , but also the hypernucleus  ${}^3_{\Lambda}\text{H}$ . The Wigner function formalism has been implemented for  $A = 3$  nuclei using realistic wave functions based on the pair-correlated hyperspherical harmonics (PHH) method [37]. For 2-body nucleon-nucleon (NN) interactions, the Argonne  $v_{18}$  potential (AV18) [38] is used, together with the Urbana IX (UIX) 3-body interaction [39]. Furthermore, the Minnesota potential [40] is tested as a simple 2-body potential which is able to reproduce the binding energy  ${}^3\text{He}$  and  ${}^3\text{H}$ . For  ${}^3_{\Lambda}\text{H}$ , two approaches are considered: The Congleton [41] approach is a simplified model of the  ${}^3_{\Lambda}\text{H}$ , with a deuteron at its core, modeled using the Argonne  $v_{18}$  wave function of the deuteron, and a shallowly bound  $\Lambda$ . The parameters of this model were tuned to reproduce modern form factor calculations [24, 42]. The second approach is based on central Gaussian interactions, including 2 and 3-body potentials [43]. The parameters of the 2-body potentials are tuned to reproduce experimental scattering lengths and effective ranges in the NN case as well as the ones from  $\chi\text{EFT}$  in the N- $\Lambda$  case. The parameters of the 3-body potential are chosen to match a binding energy of  $B({}^3_{\Lambda}\text{H}) = 2.40$  MeV. The  ${}^3_{\Lambda}\text{H}$  wave function is calculated employing the hyperspherical harmonic method [37, 44]. Details of this calculation are discussed in this paper.

---

<sup>1</sup>More precisely, the one dimensional radius assuming a gaussian source profile decreases with the average particle pair transverse momentum,  $k_T$ .

## 2 Coalescence approach for $A = 3$ nuclei

The momentum spectra of light (anti)(hyper)nuclei<sup>2</sup> with mass number  $A = 3$ , such as  ${}^3\text{H}$ ,  ${}^3\text{He}$ , and  ${}^3_{\Lambda}\text{H}$ , can be computed using the coalescence formalism. In this framework, light nuclei are assumed to form in high-energy hadronic collisions through the coalescence of nucleons and hyperons. A key assumption is that interactions between coalescing hadrons and non-participating hadrons are subdominant. We develop a coalescence model for  $A = 3$  light nuclei based on the state-of-the-art Wigner function formalism [26, 27]. We compute Lorentz-invariant momentum spectra of  ${}^3\text{H}$ ,  ${}^3\text{He}$ , and  ${}^3_{\Lambda}\text{H}$  using the three-particle density matrix formalism as follows:<sup>3</sup>

$$\gamma \frac{dN_A}{d^3P} = \frac{S_A}{(2\pi)^4} \int d^4x_1 \int d^4x_2, \int d^4x_3 \int d^4x'_1 \int d^4x'_2 \int d^4x'_3 \\ \times \Psi^*(x'_1, x'_2, x'_3) \Psi(x_1, x_2, x_3) \rho_{1,2,3}(x_1, x_2, x_3; x'_1, x'_2, x'_3), \quad (1)$$

where  $\Psi(x_1, x_2, x_3)$  is the three-particle bound state Bethe Salpeter amplitude and  $\rho_{1,2,3}$  is the three-particle reduced density matrix, while  $S_A$  accounts for the spin and isospin statistics for all three cases. The density matrix for three particle systems is assumed to be factored into single particle densities [24],  $\rho_{1,2,3}(x_1, x_2, x_3; x'_1, x'_2, x'_3) = \rho_1(x_1; x'_1) \times \rho_1(x_2; x'_2) \times \rho_1(x_3; x'_3)$ , and the single-particle density is written in terms of the single particle Wigner function,  $f_1^W$ . One can make the assumption

$$\rho_1(x, x') = \int \frac{d^4p}{(2\pi)^4} e^{ip \cdot (x' - x)} f_1^W \left( p, \frac{x + x'}{2} \right). \quad (2)$$

Furthermore, the three-particle normalized Wigner density function,  $W_A$ , can be defined as a product of single-particle Winger density functions

$$W_A \left( p_1, p_2, p_3, \frac{x_1 + x'_1}{2}, \frac{x_2 + x'_2}{2}, \frac{x_3 + x'_3}{2} \right) = \prod_{i=1}^3 f_1^W \left( p_i, \frac{x_i + x'_i}{2} \right). \quad (3)$$

At this stage, making both the low-energy approximation and the equal-time approximation (see App. A), Eq. (1) takes the form of a yield equation for  $A = 3$  cluster in three-dimensional space. The yield in three-dimensional space is written as

$$\frac{dN_A}{d^3P} = \frac{S_A}{(2\pi)^{12}} \int d^3\mathbf{p}_1 \int d^3\mathbf{p}_2 \int d^3\mathbf{p}_3 \int d^3\mathbf{x}_1 \int d^3\mathbf{x}_2 \int d^3\mathbf{x}_3 \int d^3\mathbf{x}'_1 \int d^3\mathbf{x}'_2 \int d^3\mathbf{x}'_3 \\ \times \Psi_{NR}^*(\mathbf{x}'_1, \mathbf{x}'_2, \mathbf{x}'_3) \Psi_{NR}(\mathbf{x}_1, \mathbf{x}_2, \mathbf{x}_3) e^{-i\mathbf{p}_1 \cdot (\mathbf{x}_1 - \mathbf{x}'_1) - i\mathbf{p}_2 \cdot (\mathbf{x}_2 - \mathbf{x}'_2) - i\mathbf{p}_3 \cdot (\mathbf{x}_3 - \mathbf{x}'_3)} \\ \times W_A \left( \mathbf{p}_1, \mathbf{p}_2, \mathbf{p}_3, \frac{\mathbf{x}_1 + \mathbf{x}'_1}{2}, \frac{\mathbf{x}_2 + \mathbf{x}'_2}{2}, \frac{\mathbf{x}_3 + \mathbf{x}'_3}{2} \right), \quad (4)$$

where  $\Psi_{NR}$  is the non-relativistic wave function of the nucleus under study. In general, it can be factorized into the plane wave for center-of-mass motion with total momentum  $\mathbf{P}_A$  and an internal wave function that depends only on two relative coordinates  $\boldsymbol{\xi}_1, \boldsymbol{\xi}_2$  describing the motion of internal nucleons or  $\Lambda$  relative to the center of mass,

$$\Psi_{NR}(\mathbf{x}_1, \mathbf{x}_2, \mathbf{x}_3) = (2\pi)^{-3/2} e^{i\mathbf{P}_A \cdot \mathbf{R}} \varphi_{NR}(\boldsymbol{\xi}_1, \boldsymbol{\xi}_2), \quad (5)$$

The relative Jacobi coordinates,  $\boldsymbol{\xi}_1, \boldsymbol{\xi}_2$  are defined in terms of the constituents absolute coordinates  $\mathbf{x}_1, \mathbf{x}_2$ , and  $\mathbf{x}_3$ , as well as the masses of the three particles  $m_1, m_2$ , and  $m_3$ . Moreover,  $\mathbf{R}$  represents the center-of-mass coordinate. The internal cluster wave function is denoted by  $\varphi_{NR}(\boldsymbol{\xi}_1, \boldsymbol{\xi}_2)$ . Considerations regarding the choice of Jacobi coordinates for  $A = 3$  systems are discussed in subsequent parts of this paper.

Let us first consider a system consisting of two identical particles with masses  $m_1 = m_2 = M$  and a third particle with a different mass  $m_3$ . We define the mass ratio as  $\kappa = \frac{m_3}{M}$  so that the cases of  ${}^3\text{He}$

<sup>2</sup>The formation mechanism is assumed to be the same for nuclei and their antimatter counterpart, as well as for hypernuclei. In the following, the (anti) and (hyper) prefixes will be omitted.

<sup>3</sup>Note that in these calculations, we use bold and italic fonts for three- and four-vectors.

and  ${}^3\text{H}$  can be simply recovered by setting  $\kappa = 1$  and the case of  ${}^3_{\Lambda}\text{H}$  by setting  $\kappa = \frac{m_{\Lambda}}{M} \approx 1.188$  in the final expressions. The Jacobi vectors are

$$\mathbf{R} = \frac{\mathbf{x}_1 + \mathbf{x}_2 + \kappa\mathbf{x}_3}{2 + \kappa}, \quad \boldsymbol{\xi}_2 = \mathbf{x}_2 - \mathbf{x}_1, \quad \text{and} \quad \boldsymbol{\xi}_1 = \sqrt{\frac{4\kappa}{2 + \kappa}} \left( \mathbf{x}_3 - \frac{\mathbf{x}_1 + \mathbf{x}_2}{2} \right), \quad (6)$$

$$\begin{pmatrix} \boldsymbol{\xi}_1 \\ \boldsymbol{\xi}_2 \\ \mathbf{R} \end{pmatrix} = J \times \begin{pmatrix} \mathbf{x}_1 \\ \mathbf{x}_2 \\ \mathbf{x}_3 \end{pmatrix}, \quad \begin{pmatrix} \mathbf{x}_1 \\ \mathbf{x}_2 \\ \mathbf{x}_3 \end{pmatrix} = J^{-1} \times \begin{pmatrix} \boldsymbol{\xi}_1 \\ \boldsymbol{\xi}_2 \\ \mathbf{R} \end{pmatrix}, \quad \text{and} \quad J = \begin{pmatrix} -\frac{1}{2}\sqrt{\frac{4\kappa}{2+\kappa}} & -\frac{1}{2}\sqrt{\frac{4\kappa}{2+\kappa}} & \sqrt{\frac{4\kappa}{2+\kappa}} \\ -1 & 1 & 0 \\ \frac{1}{2+\kappa} & \frac{1}{2+\kappa} & \frac{\kappa}{2+\kappa} \end{pmatrix}, \quad (7)$$

with an absolute value of the determinant as  $|J| = \sqrt{\frac{4\kappa}{2+\kappa}}$ . In terms of the Jacobi coordinates,

$$\mathbf{x}_{13} = -\sqrt{\frac{2+\kappa}{4\kappa}}\boldsymbol{\xi}_1 - \frac{1}{2}\boldsymbol{\xi}_2, \quad \mathbf{x}_{32} = \sqrt{\frac{2+\kappa}{4\kappa}}\boldsymbol{\xi}_1 - \frac{1}{2}\boldsymbol{\xi}_2. \quad (8)$$

The associated Jacobi momenta are

$$\mathbf{P} = \mathbf{p}_1 + \mathbf{p}_2 + \mathbf{p}_3, \quad \mathbf{k}_2 = \frac{1}{2}[\mathbf{p}_2 - \mathbf{p}_1], \quad \mathbf{k}_1 = \sqrt{\frac{\kappa}{2+\kappa}} \left[ \frac{\mathbf{p}_3}{\kappa} - \frac{\mathbf{p}_1 + \mathbf{p}_2}{2} \right]. \quad (9)$$

The positions and momenta in terms of the Jacobi coordinates and momenta are

$$\mathbf{x}_1 = \mathbf{R} - \frac{1}{2}\sqrt{\frac{\kappa}{2+\kappa}}\boldsymbol{\xi}_1 + \frac{\boldsymbol{\xi}_2}{2}, \quad \mathbf{p}_1 = \frac{1}{2+\kappa}\mathbf{P} - \frac{1}{2}\sqrt{\frac{4\kappa}{2+\kappa}}\mathbf{k}_1 + \mathbf{k}_2 \quad (10)$$

$$\mathbf{x}_2 = \mathbf{R} - \frac{1}{2}\sqrt{\frac{\kappa}{2+\kappa}}\boldsymbol{\xi}_1 - \frac{\boldsymbol{\xi}_2}{2}, \quad \mathbf{p}_2 = \frac{1}{2+\kappa}\mathbf{P} - \frac{1}{2}\sqrt{\frac{4\kappa}{2+\kappa}}\mathbf{k}_1 - \mathbf{k}_2 \quad (11)$$

$$\mathbf{x}_3 = \mathbf{R} + \frac{1}{\kappa}\sqrt{\frac{\kappa}{2+\kappa}}\boldsymbol{\xi}_1, \quad \mathbf{p}_3 = \frac{\kappa}{2+\kappa}\mathbf{P} + \sqrt{\frac{4\kappa}{2+\kappa}}\mathbf{k}_1. \quad (12)$$

It is easy to show that

$$\mathbf{x}_1 \cdot \mathbf{p}_1 + \mathbf{x}_2 \cdot \mathbf{p}_2 + \mathbf{x}_3 \cdot \mathbf{p}_3 = \mathbf{R} \cdot \mathbf{P} + \boldsymbol{\xi}_1 \cdot \mathbf{k}_1 + \boldsymbol{\xi}_2 \cdot \mathbf{k}_2. \quad (13)$$

The complete form of the Wigner function  $W_{\Lambda}$  is theoretically unknown [26]. However, by assuming a transition from a fully quantum mechanical treatment to a semi-classical picture and a factorization of the spatial and momentum coordinates the Wigner function  $W_{\Lambda}$  can be expressed as the product of two normalized functions: the spatial distribution  $H_{\Lambda}$  and the momentum distribution  $G_{\Lambda}$  of the coalescing hadrons

$$W_{\Lambda}(\mathbf{p}_1, \mathbf{p}_2, \mathbf{p}_3, \mathbf{x}_1, \mathbf{x}'_1, \mathbf{x}_2, \mathbf{x}'_2, \mathbf{x}_3, \mathbf{x}'_3) = H_{\Lambda}(\mathbf{x}_1, \mathbf{x}'_1, \mathbf{x}_2, \mathbf{x}'_2, \mathbf{x}_3, \mathbf{x}'_3) G_{\Lambda}(\mathbf{p}_1, \mathbf{p}_2, \mathbf{p}_3), \quad (14)$$

where function  $H_{\Lambda}$  is assumed to be the product of Gaussian distributions  $H_{\Lambda} = \prod_{i=1}^{\Lambda} h(x_i)$  and  $h(x_i)$  is a normalized Gaussian distribution,

$$h(\mathbf{x}) = (2\pi\sigma^2)^{-3/2} \exp\left\{-\frac{\mathbf{x}^2}{2\sigma^2}\right\}. \quad (15)$$

The width parameters  $\sigma$  is related to the particle emission profile and can be obtained from two-particle femtoscopic source studies in ultra-high-energy hadronic collisions [9, 45, 46]. The function  $G_{\Lambda}$  is still not known theoretically; however, since it is a distribution related to the momentum spectra of the individual nucleons, the values of this function can be incorporated by employing the event generators [26].

## 2.1 Generalized 3-body coalescence approach

In the following, we will derive the calculation of the coalescence probability for  ${}^3_{\Lambda}\text{H}$ . This defines a generalized approach for 2 equal (nucleons) and one different (hyperon) particle. Under the assumption that the third particle is equal to the other two, the cases of  ${}^3\text{He}$  and  ${}^3\text{H}$  are derived. We consider two distinct approaches for hypertriton wave function calculations. The first employs the state-of-the-art hyperspherical harmonics (HH) approach [37, 44] to solve the three-body bound-state Schrödinger equation, utilizing model Gaussian p- $\Lambda$  potentials devised in Ref. [43]. These potentials are constructed such to reproduce the low-energy scattering data as obtained from realistic hyperon-nucleon interactions devised within a chiral effective field theory framework [47, 48, 49]. These latter interactions are constrained by the available N- $\Lambda$  scattering data [50] and the latest femtoscopic measurements of the p- $\Lambda$  correlation function [50]. Although rather simple, with the inclusion of N-N- $\Lambda$  three-body potentials chosen to reproduce the hypertriton binding energy, these Gaussian potentials well describe both p- $\Lambda$  and p-p- $\Lambda$  correlation functions [43]. In addition to them, we have also considered the N- $\Lambda$  and N-N- $\Lambda$  potentials devised in Ref. [51, 52]. The precise form of the potentials and the HH method to compute the wave functions is discussed in detail in Appendix B. The second approach is based on the work developed by Congleton et al. [41], as motivated in Ref. [53].

The Wigner density matrix for the system of np $\Lambda$  appearing in Eq. (51) can be written as

$$W_{\text{np}\Lambda} \left( \mathbf{p}_1, \mathbf{p}_2, \mathbf{p}_3, \frac{\mathbf{x}_1 + \mathbf{x}'_1}{2}, \frac{\mathbf{x}_2 + \mathbf{x}'_2}{2}, \frac{\mathbf{x}_3 + \mathbf{x}'_3}{2} \right) = \frac{1}{(2\pi\sigma^2)^3} e^{-\frac{(\mathbf{x}_1 + \mathbf{x}'_1)^2 + (\mathbf{x}_2 + \mathbf{x}'_2)^2}{8\sigma^2}} \quad (16)$$

$$\times \frac{1}{(2\pi\sigma'^2)^{3/2}} e^{-\frac{(\mathbf{x}_3 + \mathbf{x}'_3)^2}{8\sigma'^2}} G_{\text{np}\Lambda}(\mathbf{p}_1, \mathbf{p}_2, \mathbf{p}_3), \quad (17)$$

where  $\sigma$  and  $\sigma'$  represent the femtoscopic source sizes for N-N pairs and N- $\Lambda$  pairs, respectively, and are assumed to be independent of each other. The values of  $\sigma$  and  $\sigma'$  are constrained by recent source size measurements and can be obtained from event generators, which are tuned to reproduce the experimental source size measurements; more details are discussed in the subsequent sections.

In the following, we define  $\tau = (\sigma/\sigma')^2$ . With this definition, one obtains

$$e^{-\frac{(\mathbf{x}_1 + \mathbf{x}'_1)^2 + (\mathbf{x}_2 + \mathbf{x}'_2)^2}{8\sigma^2}} e^{-\frac{(\mathbf{x}_3 + \mathbf{x}'_3)^2}{8\sigma'^2}} = e^{-\frac{(\mathbf{x}_1 + \mathbf{x}'_1)^2 + (\mathbf{x}_2 + \mathbf{x}'_2)^2 + \tau(\mathbf{x}_3 + \mathbf{x}'_3)^2}{8\sigma^2}}. \quad (18)$$

The exponent of Eq. (18) can be expressed in terms of  $\kappa$ ,  $\tau$ , and dummy variables  $\mathbf{t}$  and  $\alpha$

$$(\mathbf{x}_1 + \mathbf{x}'_1)^2 + (\mathbf{x}_2 + \mathbf{x}'_2)^2 + \tau(\mathbf{x}_3 + \mathbf{x}'_3)^2 = (2 + \tau) \left[ (\mathbf{R} + \mathbf{R}')^2 + 2(\mathbf{R} + \mathbf{R}') \cdot \mathbf{t} \right] + \frac{\alpha}{2} (\boldsymbol{\xi}_1 + \boldsymbol{\xi}'_1)^2 + \frac{1}{2} (\boldsymbol{\xi}_2 + \boldsymbol{\xi}'_2)^2, \quad (19)$$

where  $\mathbf{t}$  and  $\alpha$  are defined as

$$\mathbf{t} = \frac{\tau - \kappa}{\kappa(2 + \tau)} \sqrt{\frac{\kappa}{2 + \kappa}} (\boldsymbol{\xi}_1 + \boldsymbol{\xi}'_1), \quad \alpha = \frac{\kappa^2 + 2\tau}{\kappa(2 + \kappa)}. \quad (20)$$

As discussed before, the wave function for the  ${}^3_{\Lambda}\text{H}$  nucleus can be written in terms of the center-of-mass motion and an internal wave function as

$$\Psi_{NR}(\mathbf{x}_1, \mathbf{x}_2, \mathbf{x}_3) = (2\pi)^{-3/2} e^{i\mathbf{P}_{\Lambda\text{H}} \cdot \mathbf{R}} \varphi_{\Lambda\text{H}}^3(\boldsymbol{\xi}_1, \boldsymbol{\xi}_2), \quad (21)$$

where  $\varphi_{\Lambda\text{H}}^3$  is the internal part of the  ${}^3_{\Lambda}\text{H}$  wave function, describing the dynamics of the p, n, and  $\Lambda$  and  $\boldsymbol{\xi}_1$  and  $\boldsymbol{\xi}_2$  are the hyperspherical coordinates defined above. In Eq. (4) changing the integration variables from the particle positions and momenta to the center-of-mass and Jacobi coordinates, one obtains

$$\frac{dN_{\Lambda\text{H}}^3}{d^3P} = S_{\Lambda\text{H}}^3 \frac{|J^{-1}|^3}{(2\pi)^{15}} \int d^3R d^3\xi_1 d^3\xi_2 \int d^3R' d^3\xi'_1 d^3\xi'_2 e^{i\mathbf{P}_{\Lambda\text{H}} \cdot (\mathbf{R} - \mathbf{R}')} \varphi_{\Lambda\text{H}}^3(\boldsymbol{\xi}'_1, \boldsymbol{\xi}'_2) \varphi_{\Lambda\text{H}}^3(\boldsymbol{\xi}_1, \boldsymbol{\xi}_2)$$

$$\times \int d^3P d^3k_1 d^3k_2 e^{-i\mathbf{P} \cdot (\mathbf{R} - \mathbf{R}') - ik_1 \cdot (\boldsymbol{\xi}_1 - \boldsymbol{\xi}'_1) - ik_2 \cdot (\boldsymbol{\xi}_2 - \boldsymbol{\xi}'_2)}$$

$$\times \frac{\tau^{\frac{3}{2}}}{(2\pi\sigma^2)^{\frac{9}{2}}} e^{-\frac{2+\tau}{8\sigma^2} ((\mathbf{R} + \mathbf{R}')^2 + 2(\mathbf{R} + \mathbf{R}') \cdot \mathbf{t})} e^{-\frac{1}{16\sigma^2} (\alpha(\boldsymbol{\xi}_1 + \boldsymbol{\xi}'_1)^2 + (\boldsymbol{\xi}_2 + \boldsymbol{\xi}'_2)^2)} G_{\text{np}\Lambda}(\mathbf{p}_1, \mathbf{p}_2, \mathbf{p}_3), \quad (22)$$

where  $|J^{-1}| = \sqrt{(2 + \kappa)/4\kappa}$ . Furthermore, by substituting  $\mathbf{R}$  and  $\mathbf{R}'$  with the variables  $\mathbf{Z} = \mathbf{R} + \mathbf{R}'$  and  $\mathbf{Z}' = \mathbf{R} - \mathbf{R}'$ , the integration over  $\mathbf{Z}'$  results in a factor  $(2\pi)^3 \delta(\mathbf{P} - \mathbf{P}_{\Lambda}^3)$ , while the integral over  $\mathbf{Z}$  results in

$$\int d^3 Z e^{-\frac{2+\tau}{8\sigma^2}[Z^2+2\mathbf{t}\cdot\mathbf{Z}]} = \int d^3 Z e^{-\frac{2+\tau}{8\sigma^2}[(\mathbf{Z}+\mathbf{t})^2-t^2]} = \left(\frac{8\pi\sigma^2}{2+\tau}\right)^{\frac{3}{2}} e^{\frac{2+\tau}{8\sigma^2}t^2}. \quad (23)$$

Using these results, Eq. (22) becomes

$$\begin{aligned} \frac{dN_{\Lambda}^3}{d^3 P} &= S_{\Lambda}^3 \frac{|J^{-1}|^3}{(2\pi)^{12}} \int d^3 \xi_1 d^3 \xi_2 \int d^3 \xi'_1 d^3 \xi'_2 \varphi_{\Lambda}^* (\boldsymbol{\xi}'_1, \boldsymbol{\xi}'_2) \varphi_{\Lambda} (\boldsymbol{\xi}_1, \boldsymbol{\xi}_2) \\ &\times \int d^3 k_1 d^3 k_2 e^{-i\mathbf{k}_1 \cdot (\boldsymbol{\xi}_1 - \boldsymbol{\xi}'_1) - i\mathbf{k}_2 \cdot (\boldsymbol{\xi}_2 - \boldsymbol{\xi}'_2)} \\ &\times \frac{\tau^{\frac{3}{2}}}{(2\pi\sigma^2)^{\frac{9}{2}}} e^{\frac{2+\kappa}{8\sigma^2}t^2} e^{-\frac{1}{16\sigma^2}(\alpha(\boldsymbol{\xi}_1 + \boldsymbol{\xi}'_1)^2 + (\boldsymbol{\xi}_2 + \boldsymbol{\xi}'_2)^2)} G_{np\Lambda}(\mathbf{p}_1, \mathbf{p}_2, \mathbf{p}_3)|_{\mathbf{P}=\mathbf{P}_{\Lambda}^3}. \end{aligned} \quad (24)$$

Similar to Eq. (20), the following substitutions are applied

$$\frac{2+\tau}{8\sigma^2}t^2 - \frac{\alpha}{16\sigma^2}(\boldsymbol{\xi}_1 + \boldsymbol{\xi}'_1)^2 = \frac{\alpha'}{16\sigma^2}(\boldsymbol{\xi}_1 + \boldsymbol{\xi}'_1)^2, \quad \alpha' = \frac{\tau(2+\kappa)}{\kappa(2+\tau)}. \quad (25)$$

This is useful to define a compact form of the expression, which allows for the evaluation of the probability of cluster formations as given below.

$$\frac{dN_{\Lambda}^3}{d^3 P} = \frac{S_{\Lambda}^3}{(2\pi)^{12}} \int d^3 k_1 d^3 k_2 G_{np\Lambda}(\mathbf{p}_1, \mathbf{p}_2, \mathbf{p}_3)|_{\mathbf{P}=\mathbf{P}_H} \mathcal{P}(\mathbf{k}_1, \mathbf{k}_2, \sigma, \sigma'), \quad (26)$$

where

$$\begin{aligned} \mathcal{P}(\mathbf{k}_1, \mathbf{k}_2, \sigma, \sigma') &= \frac{(\alpha')^{\frac{3}{2}}}{8(2\pi)^3 \sigma^6} \int d^3 \xi_1 d^3 \xi_2 \int d^3 \xi'_1 d^3 \xi'_2 \varphi_{\Lambda}^* (\boldsymbol{\xi}'_1, \boldsymbol{\xi}'_2) \varphi_{\Lambda} (\boldsymbol{\xi}_1, \boldsymbol{\xi}_2) \\ &\times e^{-i\mathbf{k}_1 \cdot (\boldsymbol{\xi}_1 - \boldsymbol{\xi}'_1) - i\mathbf{k}_2 \cdot (\boldsymbol{\xi}_2 - \boldsymbol{\xi}'_2)} e^{-\frac{1}{16\sigma^2}(\alpha'(\boldsymbol{\xi}_1 + \boldsymbol{\xi}'_1)^2 + (\boldsymbol{\xi}_2 + \boldsymbol{\xi}'_2)^2)}. \end{aligned} \quad (27)$$

Using realistic numbers and Eq. 25, we can approximate  $\alpha'$  such that

$$\sigma_{p\Lambda} = \frac{1}{\sqrt{2}} \sqrt{\sigma_p^2 + \sigma_{\Lambda}^2} \simeq 1.15\sigma_p \text{ [45]} \Leftrightarrow \sigma_{\Lambda}^2 \simeq 1.645\sigma_p^2 \quad (28)$$

$$\tau = (\sigma_p/\sigma_{\Lambda})^2 \simeq 0.608 \Rightarrow \alpha' \simeq 0.626 \quad (29)$$

As a test,  $\mathcal{P}(\mathbf{0}, \mathbf{0}, \sigma \rightarrow 0, \sigma' = \sigma\sqrt{\tau})$  can be computed. In such a case, the Gaussians become delta functions, namely

$$e^{-\frac{1}{16\sigma^2}(\alpha'(\boldsymbol{\xi}_1 + \boldsymbol{\xi}'_1)^2 + (\boldsymbol{\xi}_2 + \boldsymbol{\xi}'_2)^2)} \rightarrow \left(\frac{16\pi\sigma^2}{\sqrt{\alpha'}}\right)^3 \delta(\boldsymbol{\xi}_1 + \boldsymbol{\xi}'_1) \delta(\boldsymbol{\xi}_2 + \boldsymbol{\xi}'_2), \quad \sigma \rightarrow 0. \quad (30)$$

Inserting this expression in Eq. (27), and applying the normalization condition of the wave function  $\int d^3 \xi_1 d^3 \xi_2 |\varphi_{\Lambda}^3(\boldsymbol{\xi}_1, \boldsymbol{\xi}_2)|^2 = 1$ , we obtain

$$\mathcal{P}(\mathbf{0}, \mathbf{0}, 0, 0) = 64. \quad (31)$$

This is the expected value since the Wigner function  $\mathcal{D}(0, 0, 0, 0) = 64$  by definition. This cross-check shows that the normalization as well as all prefactors are applied properly.

A complete description of the calculation of  $\varphi_{\Lambda}^3$  using the PHH method is provided in the Appendix. B. The case of  ${}^3\text{He}$  and  ${}^3\text{H}$  can be recovered by setting  $\kappa = 1$  and  $\tau = 1$ , from which follows that  $\alpha' = 1$  in Eq. 27. Details of the  ${}^3\text{He}$  and  ${}^3\text{H}$  wave functions can also be found in Appendix B.

## 2.2 Congleton approach for Hypertriton

A second approach for calculating the  ${}^3_\Lambda\text{H}$  yield has been developed based on the Congleton wave function [41]. This is a relatively simple approach for determining the  ${}^3_\Lambda\text{H}$  wave function, where the  $\Lambda$  particle is assumed to orbit an unperturbed deuteron in a  $\Lambda$ -d potential ( $V_{\Lambda-d}$ ). This potential is based on a separable N- $\Lambda$  interaction. The governing Hamiltonian for the system, including center-of-mass motion, is given by

$$\begin{aligned} H &= \frac{p^2}{2m_\mu} + V_{\text{np}} + \frac{q^2}{2\mu} + V_{\Lambda-d} \\ &= H_d(\mathbf{p}) + V_\Lambda(\mathbf{q}). \end{aligned} \quad (32)$$

The Hamiltonian is split into two parts using a static approximation, in which the effective  $\Lambda$ -d system is considered. This way, the influence of the  $\Lambda$  particle on the individual nucleons is neglected. Consequently, the  $V_{\Lambda-d}$  potential depends only on the variable  $\mathbf{q}$  (after accounting for spin dependence). Furthermore, the reduced mass of the  $\Lambda$ -d system is  $\mu = 3.547 \text{ fm}^{-1}$  while the reduced mass of the two-nucleon system is  $m_\mu = 2.379 \text{ fm}^{-1}$ .

The wave function can be expressed as the product of the spin function ( $s = \frac{1}{2}$  for Hypertriton) and the nuclear wave function part

$$\langle \mathbf{p}, \mathbf{q} | {}^3_\Lambda H; m_j \rangle = \psi_\Lambda(q) \sum_{(l,s)=(0,\frac{1}{2}), (2,\frac{3}{2})} \psi_d^{(l)}(p) \times \left[ \mathcal{Y}'_{l0}(\hat{p}, \hat{q}) \otimes \chi_{1\frac{1}{2}}^S \right]_{\frac{1}{2} m_j} \frac{1}{\sqrt{2}} [\Lambda(\uparrow\downarrow - \downarrow\uparrow)], \quad (33)$$

where  $\psi_\Lambda(q)$  and  $\psi_d^{(l)}(p)$  represent the  $\Lambda$  wave function and the radial part of the deuteron wave function in the momentum space, respectively. The spin component describes the coupling between the spin-1 deuteron and the spin- $\frac{1}{2}$   $\Lambda$  particle, resulting in a total spin of either  $\frac{1}{2}$  or  $\frac{3}{2}$ . The  $s$ -wave component of the deuteron corresponds to  $S = \frac{1}{2}$ , while the  $d$ -wave component corresponds to  $S = \frac{3}{2}$ . Apart from the spin component, the spatial wave function is a simple product of the deuteron and  $\Lambda$  wave functions. Similar to the HH approach, the total wave function for the hypertriton  $\Psi_{\Lambda\text{H}}(\mathbf{x}_1, \mathbf{x}_2, \mathbf{x}_3)$  can be factorized into a plane wave for the center-of-mass (COM) motion and an internal wave function that depends only on two relative coordinates, as shown in Eq. 21. The internal wave function is given as the product of  $\Lambda$  and deuteron wave functions.

$$\varphi_{\Lambda\text{H}}(\boldsymbol{\xi}_1, \boldsymbol{\xi}_2) = \varphi_\Lambda(\boldsymbol{\xi}_1) \times \varphi_d(\boldsymbol{\xi}_2), \quad (34)$$

where,  $\varphi_\Lambda(\boldsymbol{\xi}_1)$  and  $\varphi_d(\boldsymbol{\xi}_2)$  are the corresponding Fourier transform of the momentum space wave functions  $\psi_\Lambda(q)$  and  $\psi_d^{(l)}(p)$  respectively. The final probability is given in terms of the Wigner functions for deuteron and for the  $\Lambda$ -d two-body system as

$$\mathcal{P}(\mathbf{k}_1, \mathbf{k}_2, \sigma) = \frac{(2 + \kappa^2)^{3/2}}{(2 + \kappa)^3} \frac{S_{\Lambda\text{H}}^3}{(2\pi)^3 \sigma^6} \int d^3 r_1 \int d^3 r_2 \mathcal{D}_\Lambda(\mathbf{k}_1, \mathbf{r}_1) \mathcal{D}_d(\mathbf{k}_2, \mathbf{r}_2) e^{-\frac{r_1^2(2+\kappa)^2 + 4r_2^2(2+\kappa^2)}{4\sigma^2(2+\kappa)^2}}. \quad (35)$$

The Wigner densities of the  $\Lambda$  particle denoted as  $\mathcal{D}_\Lambda(\mathbf{k}_1, \mathbf{r}_1)$  is calculated in momentum space and the deuteron one,  $\mathcal{D}_d(\mathbf{k}_2, \mathbf{r}_2)$ , is computed in coordinate space. The computation of  $\mathcal{D}_d(\mathbf{k}_2, \mathbf{r}_2)$  has already been provided in a previous work [27], using the Argonne  $v_{18}$  wave function, while the derivation of  $\mathcal{D}_\Lambda(\mathbf{k}_1, \mathbf{r}_1)$  is given in Appendix C. The radial  $\Lambda$  wave function in momentum space is then given by [41]

$$\psi_\Lambda(q) = N(Q_\Lambda) \frac{e^{-\left(\frac{q}{Q_\Lambda}\right)^2}}{q^2 + \alpha_\Lambda^2}, \quad (36)$$

where  $N(Q_\Lambda)$  is a normalization constant

$$N(Q_\Lambda) = \left\{ \frac{\pi}{4\alpha_\Lambda} \left[ \left( \frac{4\alpha_\Lambda^2}{Q_\Lambda^2} + 1 \right) \text{Cerfe} \left( \frac{\sqrt{2}\alpha_\Lambda}{Q_\Lambda} \right) - \frac{2\alpha_\Lambda \left( \frac{2}{\pi} \right)^{1/2}}{Q_\Lambda} \right] \right\}^{-1/2}. \quad (37)$$

The **Cerfe** function is defined as  $\text{Cerfe}(x) = \exp(x^2)(1 - \text{erf}(x))$ . In the original publication [41] the parameter  $\alpha_\Lambda = \sqrt{\mu B_\Lambda} = 0.068 \text{ fm}^{-1}$  was fixed to the binding energy and  $Q_\Lambda = 1.17 \text{ fm}^{-1}$  was

adjusted to the  $\Lambda$  separation energy. In Ref. [24], the parameter  $Q_\Lambda$  of the wave function was adjusted to match the form factor of Hildenbrand&Hammer [42] obtained from pionless effective field theory. An excellent agreement is reached when  $Q_\Lambda = 2.5 \text{ fm}^{-1}$  instead of  $Q_\Lambda = 1.17 \text{ fm}^{-1}$ . With these parameters  $N(Q_\Lambda = 2.5 \text{ fm}^{-1})^2 = 0.094$  and  $\int |\psi_\Lambda(q)|^2 d^3q = 4\pi$ . The final Wigner function  $\mathcal{D}_\Lambda(\mathbf{q}, \mathbf{r})$  is given as

$$\mathcal{D}_\Lambda(\mathbf{q}, \mathbf{r}) = N(Q_\Lambda)^2 \int_0^\infty dk \frac{4i\pi (-1 + e^{2ikr})}{qr (k^2 + 4(\alpha_\Lambda^2 + q^2))} \log \left( \frac{4\alpha_\Lambda^2 + (k - 2q)^2}{4\alpha_\Lambda^2 + (k + 2q)^2} \right) e^{-\frac{k^2 + 2ikQ_\Lambda^2 r + 4q^2}{2Q_\Lambda^2}}, \quad (38)$$

and  $\mathcal{D}_\Lambda(0, 0)/4\pi = 8.0$  as expected given the normalization of the wave function.

### 3 ToMCCA upgrade for $A = 3$ coalescence

For the extension of the coalescence predictions, the ToMCCA model [36] had to be upgraded to incorporate the production of  $A = 3$  nuclei. The first step is to include an additional particle loop. For  ${}^3\text{He}$  this loop adds another proton, looping over  $N_p - 1$  nucleons. Due to the isospin symmetry assumed in ToMCCA, the case of  ${}^3\text{H}$  is also covered since the first and third particles can be assumed to be neutrons. The case of  ${}^3_\Lambda\text{H}$  is slightly more complicated. Here, the third loop includes a  $\Lambda$ , which no longer abides by the isospin symmetry. The yields are modified by the  $\Lambda/p$  ratio measured by the ALICE collaboration as a function of multiplicity [54]. Due to the very similar mass of  $\Lambda$  and proton, modifications of the  $p_T$  spectral shape can be neglected. The second major change is the used phase space of nucleons. Previously, ToMCCA provided an uncorrelated phase space, including only very basic correlations between particles, which were mainly driven by angular correlations. However, fully-fledged Monte Carlo generators include more detailed correlations, especially between the spatial position and momentum of each particle. In order to incorporate these into ToMCCA, the EPOS 3<sup>4</sup> event generator was utilized, and the two-particle phase space was extracted. This means that for each nucleon-nucleon pair in the EPOS simulation, the relative momentum  $k^*$ , distance, and  $\langle m_T \rangle$  were extracted and stored. Further, each event was classified by the mid-rapidity multiplicity  $\langle dN_{\text{ch}}/d\eta \rangle_{|\eta| < 0.5}$ . This provides a 4-dimensional distribution encoding the entire two-particle correlations provided by EPOS. In ToMCCA, each pair draws its source size from this distribution once  $k^*$ ,  $N_{\text{ch}}$  and  $\langle m_T \rangle$  are determined. The phase space is assumed to be equal for nucleon-nucleon and nucleon-hyperon pairs. This leaves three different source sizes for the nucleon triplet. These three sizes are averaged according to

$$R_{\text{av}} = \sqrt{\frac{8(R_1^2 + R_2^2 + R_3^2)(R_2^2 R_3^2 + R_1^2(R_2^2 + R_3^2))^2}{3R_1 R_2 R_3 \sqrt{R_1^{-2} + R_2^{-2} + R_3^{-2}} ((R_1^2 + R_2^2)(R_1^2 + R_2^2 + 4R_3^2))^{5/2}}}, \quad (39)$$

which has been obtained by comparing the mean of the Gaussian source distribution of three equal-sized sources to one of three independent sources. This change of the phase space also requires a refitting of the source size. The source size scaling with  $\langle m_T \rangle$  has been previously parameterized as a power law

$$\sigma(\langle m_T \rangle) = B(\langle m_T \rangle)^C. \quad (40)$$

The parameters  $B$  and  $C$  also depend on  $\langle dN_{\text{ch}}/d\eta \rangle_{|\eta| < 0.5}$ <sup>5</sup>

$$B(N_{\text{ch}}) = \frac{0.693 N_{\text{ch}}^{1/3}}{1 + e^{-0.2134(N_{\text{ch}} - 15.4682)}} - \frac{1.6483}{1 + e^{-0.2134(N_{\text{ch}} - 15.4682)}} + 0.9234, \quad (41)$$

$$C(N_{\text{ch}}) = \frac{0.6152}{0.456 + e^{-2.9428 N_{\text{ch}} + 2.7995}} + 0.1525. \quad (42)$$

Similar to the previous parameterization [36], these source radii are not to be understood as a genuine prediction but an effective parameterization. Lastly, the angular correlations need to be extended to the three-particle case. The base assumption is that two-particle correlations are dominant over genuine three-particle correlations. Then, the relative angular distribution can be constructed from two-particle

<sup>4</sup>The EPOS 3.117 event generator was used with the special setting to force the impact parameter  $b = 0$ .

<sup>5</sup>for sake of readability  $\langle dN_{\text{ch}}/d\eta \rangle_{|\eta| < 0.5} \rightarrow N_{\text{ch}}$

correlations. The first particle is assigned an absolute azimuthal value from a flat distribution. Then, from the two-particle correlations used in the  $A = 2$  case, the second particle is assigned an angular distribution

$$\mathcal{P}(\varphi_2) = 1 \times (N \sin(a\Delta\varphi_{12} - b) + c), \quad (43)$$

where  $\Delta\varphi_{12} = \varphi_1 - \varphi_2$  and  $a = 1, b = \pi/2$ . The parameters  $c$  and  $N$  depend on the mean charged particle multiplicity of the event  $N_{\text{ch}}$

$$c = 0.8095 + 0.1285 \cdot N_{\text{ch}}^{0.111} \quad (44)$$

$$N = 0.406 \cdot N_{\text{ch}}^{-0.373}. \quad (45)$$

These parameters were obtained from fitting the  $\Delta\varphi$  correlation functions as a function of multiplicity obtained by the ALICE collaboration [55]. The third particle undergoes the same procedure, but this time depending on two relative angles  $\Delta\varphi_{13}$  and  $\Delta\varphi_{23}$

$$\mathcal{P}(\varphi_3) = 1 \times (N \sin(a\Delta\varphi_{13} - b) + c) \times (N \sin(a\Delta\varphi_{23} - b) + c). \quad (46)$$

## 4 Comparison to experimental data

### 4.1 ${}^3\text{He}$ and ${}^3\text{H}$ production

In this section the output of ToMCCA is compared to experimental data. The AV18+UIX wave function with a momentum cutoff of  $\Lambda_c = 1$  GeV is considered as a reference, but also other wave functions are tested and differences are discussed. Figure 1 shows the  ${}^3\text{He}$   $p_T$  spectra measured by ALICE [56] in four different  $\langle dN_{\text{ch}}/d\eta \rangle_{|\eta| < 0.5}$  intervals: i) high multiplicity (HM, blue) with  $\langle dN_{\text{ch}}/d\eta \rangle_{|\eta| < 0.5} = 31.5 \pm 0.3$ , ii) minimum bias (MB, orange) with  $\langle dN_{\text{ch}}/d\eta \rangle_{|\eta| < 0.5} = 6.9 \pm 0.1$ , and a subdivision of minimum bias into iii) MB-I (red) and iv) MB-II (purple), with  $\langle dN_{\text{ch}}/d\eta \rangle_{|\eta| < 0.5} = 18.7 \pm 0.3$  and  $6.0 \pm 0.2$  respectively. The shown experimental uncertainties are the statistical and systematic uncertainty added in quadrature. For the minimum bias predictions, the published multiplicity distributions [57] were used instead of the Erlang functions used for the multiplicity-dependent studies. The predictions from ToMCCA using the AV18+UIX wave function are shown as colored lines. Overall, an excellent agreement within  $2\sigma$  is reached with all data points.

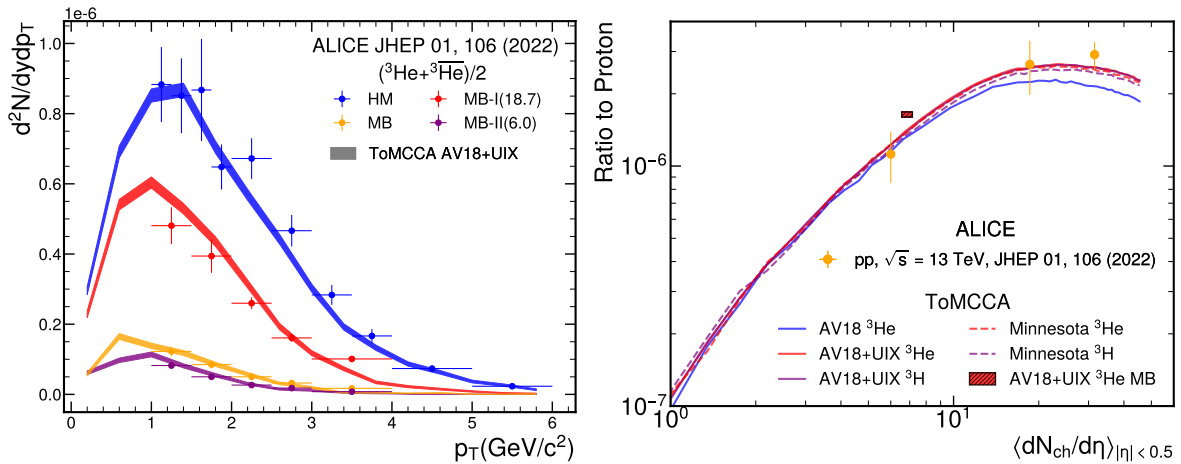


Figure 1: (left) The  ${}^3\text{He}$   $p_T$  spectra measured by ALICE [56] in pp collisions at  $\sqrt{s} = 13$  TeV in four intervals of multiplicity. The corresponding predictions for ToMCCA are shown as the colored bands. (right) The  ${}^3\text{He}/p$  ratio as a function of  $\langle dN_{\text{ch}}/d\eta \rangle_{|\eta| < 0.5}$  and comparison to the ALICE measurements [56]. Different assumptions for the wave function are tested, only 2-body forces based on the Argonne  $v_{18}$  potential (blue), 2-body+3-body Argonne  $v_{18}$  +UIX wave function for  ${}^3\text{He}$  and  ${}^3\text{H}$  as well as wave function based on the 2-body Minnesota potential. The predictions for 13 TeV minimum bias collisions is shown as the hatched box.

Reference [58] predicted that there should be a difference in production yield between  ${}^3\text{He}$  and  ${}^3\text{H}$  due to their different size ( $r_{{}^3\text{He}}/r_{{}^3\text{H}} \approx 1.11$ ), which gets more pronounced towards lower  $\langle dN_{\text{ch}}/d\eta \rangle_{|\eta| < 0.5}$  corresponding to smaller source radii. The interplay between the size of the nucleus ( $r_{{}^3\text{He}} = 1.77$  fm,  $r_{{}^3\text{H}} = 1.6$  fm) and the source size ( $\sigma \approx 1 - 1.5$  fm) causes a suppression of larger nuclei for smaller source sizes. The ToMCCA prediction of the yield ratio between  ${}^3\text{H}$  and  ${}^3\text{He}$  is shown in Fig. 2 (left) alongside the previously mentioned prediction and the only measurement in small systems by ALICE [56] in pp collisions at  $\sqrt{s} = 13$  TeV. Interestingly, ToMCCA predicts no dependence of this ratio on the source size, showing instead a constant ratio of  $0.995 \pm 0.007$  over the whole multiplicity range. The main difference between the two predictions are the nuclear wave functions. While Ref. [58] uses Gaussian wave functions, ToMCCA uses more realistic assumptions on the structure of the nuclei. Figure 2 (right) shows the effect of the 3-body force on the  ${}^3\text{He}$  and  ${}^3\text{H}$  yields. The

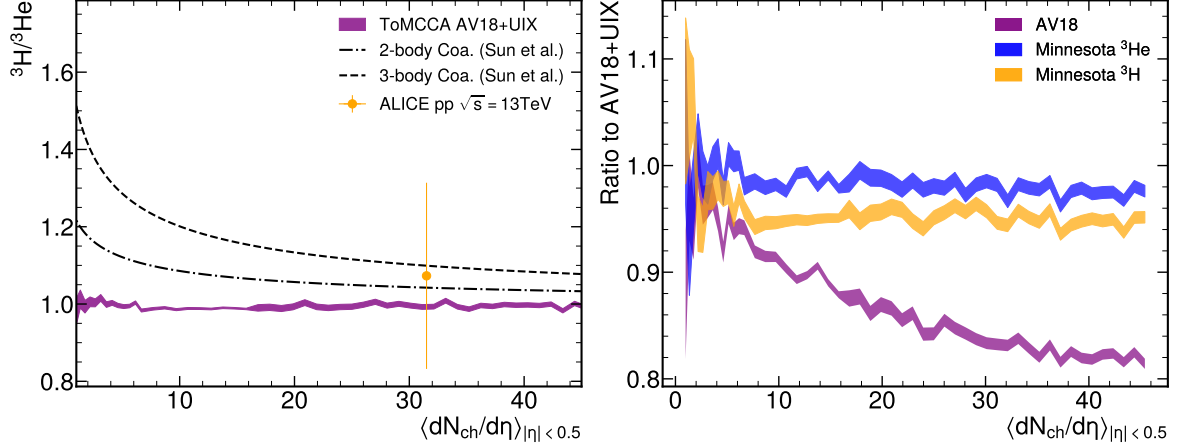


Figure 2: (left)  ${}^3\text{He}/{}^3\text{H}$  ratio as a function of multiplicity measured by ALICE in high-multiplicity pp collisions at  $\sqrt{s} = 13$  TeV. The purple band shows the predictions by ToMCCA using 2+3-body interaction in both cases, the  ${}^3\text{He}$  and the  ${}^3\text{H}$ . The dashed and dot-dashed lines indicate predictions by [58] using different assumptions of a Gaussian wave function. (right) The ratio of  ${}^3\text{He}$  using only the AV18 wave function over  ${}^3\text{He}$  using the AV18+UIX wave function as a function of multiplicity. Further the ratios of  ${}^3\text{He}$  and  ${}^3\text{H}$  obtained using the Minnesota potential to the AV18+UIX case are shown.

ratio of the  ${}^3\text{He}$  yields between AV18, which considers only the 2-body forces, and AV18/UIX, which considers 2 and 3-body forces (purple band), is close to unity for very small  $\langle dN_{\text{ch}}/d\eta \rangle_{|\eta| < 0.5}$ , with an increasing deviation towards higher multiplicities, up to 18% at  $\langle dN_{\text{ch}}/d\eta \rangle_{|\eta| < 0.5} = 45$ . This shows an enhancement of the yield when including attractive 3-body forces, reducing the size of the nucleus. The effect even gets more pronounced at larger multiplicities, corresponding to larger source sizes. This goes against the findings of Ref. [58], where the yield of the smaller nucleus (e.g.  ${}^3\text{H}$ ) compared to the larger nucleus (e.g.  ${}^3\text{He}$ ) is enhanced at low multiplicities and smaller source sizes. Similarly to the case of  ${}^3\text{H}/{}^3\text{He}$ , the size ultimately seems to not be the driving factor in nuclear production but the underlying interactions between the nucleons. Indeed, the UIX potential is mainly driven by long-range three-nucleon two-pion exchange. At larger sources, the long-range effects of the interaction become more important, and the attractive nature of the 3-body force increases the yields. Studies with other 3-body forces with varying ranges could be performed to quantify the effect of the interplay between source size and 3-body interaction range. This is relegated to future studies. Another realistic assumption for the nuclear wave function is given by the Minnesota potential [40], a simplified version of the nucleon-nucleon interaction (it does not include any tensor component). Despite its simplicity and the absence of a 3-body component, it is able to reproduce the binding energy of  ${}^3\text{He}$  and  ${}^3\text{H}$  within 1%. The ratio to the AV18+UIX wave function predictions shows that this potential is also equally able to reproduce the yields, with a ratio of  $0.984 \pm 0.016$  in the case of  ${}^3\text{He}$  and  $0.960 \pm 0.027$  in the case of  ${}^3\text{H}$ . Interestingly, the  ${}^3\text{H}$  yield is systematically lower by  $\sim (2.5 \pm 2)\%$ , which is, considering the model uncertainties (Sec. 4.3), not significant. A similar result can be seen in Fig. 1(right). It shows the  ${}^3\text{He}/p$  ratio as a function of  $\langle dN_{\text{ch}}/d\eta \rangle_{|\eta| < 0.5}$  compared to the measurements by ALICE [56]. The

ToMCCA predictions for all wave functions are shown as the colored lines and the result for the true minimum bias prediction using AV18+UIX is shown as the hatched box. All wave functions except the AV18 only assumption reproduce the measurements.

## 4.2 ${}^3_{\Lambda}\text{H}$ production

ToMCCA is extended to include hyperon production as described in Sec. 3. For the  ${}^3_{\Lambda}\text{H}$ , the Congleton wave function is used (see Sec. 2.2). Figure 3 (left) shows the  ${}^3_{\Lambda}\text{H}$   $p_T$  spectra for pp collisions in the same multiplicity classes as Fig. 1. No published spectra are available for comparisons at this time for pp collisions. Figure 3 (right) shows the  ${}^3_{\Lambda}\text{H}/{}^3\text{He}$  ratio as a function of  $p_T$ . This observable is sensitive to differences between thermal production models and coalescence models. Thermal models usually determine the  $p_T$  spectra using blast-wave parameterizations, mimicking radial flow effects. Radial flow causes heavier particles to have harder spectra, which causes this ratio to rise with  $p_T$ . On the other end, in coalescence models, the driving factor is the source size. At larger  $p_T$  a smaller source size is observed. This causes suppression of larger nuclei such as  ${}^3_{\Lambda}\text{H}$ , and hence the ratio is suppressed. It is unclear how this observation stands compared to the  ${}^3\text{H}/{}^3\text{He}$  ratio, where the size of the nuclei did not influence the result. Figure 4 (left) depicts the ratio of  ${}^3_{\Lambda}\text{H}/\Lambda$  as a function of

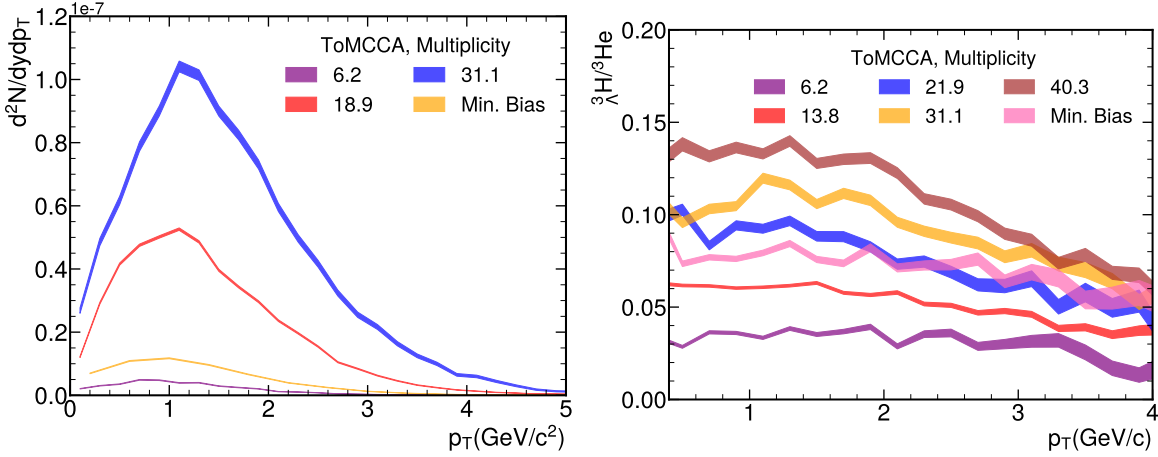


Figure 3: (left) The  ${}^3_{\Lambda}\text{H}$   $p_T$  spectra using the Congleton wave function predicted by ToMCCA for the same multiplicities in which the  ${}^3\text{He}$  measurements were performed in pp collisions at  $\sqrt{s} = 13$  TeV. No experimental data is available for comparison at this time. (right) Ratio of  ${}^3_{\Lambda}\text{H}/{}^3\text{He}$  as a function of  $p_T$  for various multiplicity classes as predicted by ToMCCA using the Congleton wave function for  ${}^3_{\Lambda}\text{H}$  and Argonne  $v_{18} + \text{UIX}$  for  ${}^3\text{He}$ .

$\langle dN_{\text{ch}}/d\eta \rangle_{|\eta| < 0.5}$ . Similarly to the  $p_T$  spectra, no integrated yields have been published for pp collisions yet. Only one measurement from p-Pb collisions is shown, however it is unclear if p-Pb and pp results should be compatible. The ToMCCA prediction is shown as the purple band. The purple box with the hatching shows the result of using the minimum bias multiplicity distribution, as used for  ${}^3\text{He}$ . The yield is  $\approx 3$  times larger than using the Erlang distribution for  $\langle dN_{\text{ch}}/d\eta \rangle_{|\eta| < 0.5} = 6.9$ , due to the much larger width of the distribution. Since coalescence is a non-linear process, i.e., it does not depend on the number of nucleons but the number of nucleon pairs, it is sensitive to higher moments of the multiplicity distribution. The right side of Fig. 4 shows the strangeness population factor  $S_3 = \frac{{}^3_{\Lambda}\text{H} \times \text{p}}{{}^3\text{He} \times \Lambda}$ . For the  ${}^3\text{He}$  predictions, the AV18+UIX was used. The predictions from Ref. [58] are shown as the dashed and dot-dashed lines. For  $S_3$  the  ${}^3\text{He}$  yield was obtained using the 3-body coalescence approach in both cases.

## 4.3 Model uncertainties

In this section, the global yield uncertainties will be discussed. From the  $A = 2$  case [36], the uncertainty on the source size, caused by the measured deuteron and proton spectra uncertainty, was 5.7%. It was obtained by varying the  $B$  parameter in Eq. 40 within the uncertainties obtained from

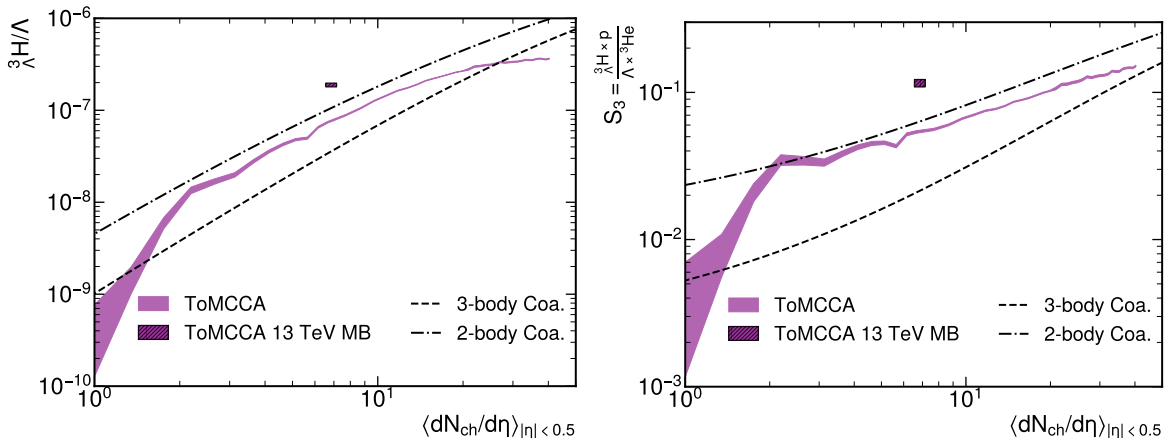


Figure 4: (left)  $\frac{{}^3\text{H}}{\Lambda}$  ratio predicted by ToMCCA using the Congleton wave function are shown as the purple band. The dashed and dot-dashed lines are predictions from [58] using different assumptions for a Gaussian wave function. (right) The purple band shows the predictions of the  $S_3$  parameter by ToMCCA using the Congleton wave function. The dashed and dot-dashed lines are the same model as on the left [58].

fitting the deuteron spectra and is thus independent of  $\langle m_T \rangle$ . When varying the source size by this amount, the  ${}^3\text{He}$  yield changed by  $\pm 13\%$  for  $\langle dN_{\text{ch}}/d\eta \rangle_{|\eta| < 0.5} = 2$  and by  $\pm 18\%$  for  $\langle dN_{\text{ch}}/d\eta \rangle_{|\eta| < 0.5} = 45$ , giving on average a variation of  $\pm 15.5\%$ . Additionally, the cutoff momentum  $\Lambda_c = 1 \text{ GeV}/c$  for the  ${}^3\text{He}$  and  ${}^3\text{H}$  wave functions was varied by  $\pm 50 \text{ MeV}$ , which resulted in a global variation of  $\pm 7\%$ . Adding these two, a global uncertainty of  $\pm 17\%$  is reached. In the case of  $\frac{{}^3\text{H}}{\Lambda}$ , the cutoff variation can be omitted, and a global uncertainty of  $\pm 15.5\%$  is taken.

## 5 Summary and Outlook

In this paper, we have presented an upgrade of the ToMCCA model to incorporate coalescence for  $A = 3$  nuclei, including  ${}^3\text{He}$ ,  ${}^3\text{H}$ , and  $\frac{{}^3\text{H}}{\Lambda}$ . The results for  ${}^3\text{He}$  and  ${}^3\text{H}$  are obtained for various different wave functions based on Argonne  $v_{18}$  for the 2-body potential and Urbana IX for the genuine 3-body potential, as well as the Minnesota potential, which is a 2-body potential capable of reproducing the binding energies without additional 3-body potentials. The results for all wave functions that reproduce the binding energies are compatible with each other, and only the Argonne  $v_{18}$  without UIX wave function shows a significant deviation. Interestingly, the  ${}^3\text{H}/{}^3\text{He}$  ratio shows no dependence on the charged-particle multiplicity, which is in contrast to previous studies using Gaussian wave functions [58]. Overall, the description of  ${}^3\text{He}$  yields and their  $p_T$  spectra is in agreement with the measurements by ALICE in pp collisions at  $\sqrt{s} = 13 \text{ TeV}$ . In the case of  $\frac{{}^3\text{H}}{\Lambda}$  the Congleton approach [41] for the wave function was tested. It includes an undisturbed deuteron, described using the Argonne  $v_{18}$  wave function, and a quasi-free  $\Lambda$  around it. With this wave function, predictions for the yields and  $p_T$  spectra in pp collisions are presented. As of now, no data on  $\frac{{}^3\text{H}}{\Lambda}$  production in pp collisions has been published. The  $\frac{{}^3\text{H}}{\Lambda}/{}^3\text{He}$  ratio is predicted by ToMCCA to drop off with increasing  $p_T$ , which is a common differentiator between thermal production and coalescence models. The minimum bias predictions of the  $\frac{{}^3\text{H}}{\Lambda}$  yield are about 3 times higher than the yield at the same mean multiplicity, but with a narrow multiplicity interval using Erlang functions.

With this successful upgrade of the ToMCCA model to  $A = 3$  coalescence it can be used for predictions of nuclei yields at different collision energies, specifically the ones interesting for indirect dark matter searches. Furthermore, the predictions could help in determining the production mechanism of light nuclei once high-precision data from the LHCs Run-3 and Run-4 campaigns become available.

## Acknowledgments

## Declarations

This work is supported by the European Research Council (ERC) under the European Union's Horizon 2020 research and innovation programme (Grant Agreement No 950692) and the BMBF 05P24W04 ALICE. The work of Bhawani Singh was partially supported by the U.S. Department of Energy, Office of Science, and Office of Nuclear Physics under contract DE-AC05-06OR23177.

## A 4D to 3D reduction

In the so-called *sudden approximation*, the Lorentz-invariant yield of a trinucleon system of total spin  $s$  is given by: <sup>6</sup>

$$\gamma \frac{dN_A}{d^3P} = \frac{S_A}{(2\pi)^4} \int d^4x_1 \int d^4x_2 \int d^4x_3 \int d^4x'_1 \int d^4x'_2 \int d^4x'_3 \times \Psi^*(x'_1, x'_2, x'_3) \Psi(x_1, x_2, x_3) \rho_{1,2,3}(x_1, x_2, x_3; x'_1, x'_2, x'_3), \quad (47)$$

where  $\Psi(x_1, x_2, x_3)$  is the three-particle bound state Bethe Salpeter amplitude and  $\rho_{1,2,3}$  is the three-particle reduced density matrix, while the factor  $S_A$  accounts for the spin and isospin statistics of the considered case. The density matrix for three particle systems is assumed to be factored into single particle densities [?]  $\rho_{1,2,3}(x_1, x_2, x_3; x'_1, x'_2, x'_3) = \rho_1(x_1; x'_1) \times \rho_1(x_2; x'_2) \times \rho_1(x_3; x'_3)$ , and the single-particle density is written in terms of single particle Wigner function,  $f_1^W$ ,

$$\rho_1(x, x') = \int \frac{d^4p}{(2\pi)^4} e^{ip \cdot (x' - x)} f_1^W\left(p, \frac{x + x'}{2}\right). \quad (48)$$

In the following, we define the three-particle normalized Wigner density function,  $W_A$ , as

$$W_A\left(p_1, p_2, p_3, \frac{x_1 + x'_1}{2}, \frac{x_2 + x'_2}{2}, \frac{x_3 + x'_3}{2}\right) = f_1^W\left(p_1, \frac{x_1 + x'_1}{2}\right) f_1^W\left(p_2, \frac{x_2 + x'_2}{2}\right) f_1^W\left(p_3, \frac{x_3 + x'_3}{2}\right), \quad (49)$$

so that the three-particle reduced density matrix can be written as

$$\rho_{1,2,3}(x_1, x_2, x_3; x'_1, x'_2, x'_3) = \frac{1}{(2\pi)^{12}} \int d^4p_1 \int d^4p_2 \int d^4p_3 e^{ip_1 \cdot (x_1 - x'_1) + ip_2 \cdot (x_2 - x'_2) + ip_3 \cdot (x_3 - x'_3)} \times W_A\left(p_1, p_2, p_3, \frac{x_1 + x'_1}{2}, \frac{x_2 + x'_2}{2}, \frac{x_3 + x'_3}{2}\right). \quad (50)$$

With this definitions, Eq. (50) reads

$$\gamma \frac{dN_A}{d^3P} = \frac{S_A}{(2\pi)^{16}} \int d^4p_1 \int d^4p_2 \int d^4p_3 \int d^4x_1 \int d^4x_2 \int d^4x_3 \int d^4x'_1 \int d^4x'_2 \int d^4x'_3 \times \Psi^*(x'_1, x'_2, x'_3) \Psi(x_1, x_2, x_3) e^{ip_1 \cdot (x_1 - x'_1) + ip_2 \cdot (x_2 - x'_2) + ip_3 \cdot (x_3 - x'_3)} \times W_A\left(p_1, p_2, p_3, \frac{x_1 + x'_1}{2}, \frac{x_2 + x'_2}{2}, \frac{x_3 + x'_3}{2}\right). \quad (51)$$

Now, we introduce the center-of-mass four vector  $R$  and a pair of Jacobi four vectors  $\xi_1, \xi_2$ , related to  $x_1, x_2, x_3$  by some linear relation which depends on the masses of the three particles. In general, we have  $x_i = R + w_{1,i}\xi_1 + w_{2,i}\xi_2$ . Moreover,  $d^4x_1 d^4x_2 d^4x_3 = |J^{-1}|^4 d^4R d^4\xi_1 d^4\xi_2$ . The conjugate four momenta of  $R, \xi_1, \xi_2$  are the total four momentum  $P = p_1 + p_2 + p_3$  and a pair of Jacobi four momenta  $q_1, q_2$ . We have  $p_1 \cdot x_1 + p_2 \cdot x_2 + p_3 \cdot x_3 = P \cdot R + \xi_1 \cdot q_1 + \xi_2 \cdot q_2$ . In general, we find  $p_i = c_i P +$  some linear combinations of  $k_1$  and  $k_2$ , where  $c_1 + c_2 + c_3 = 1$ . Finally,  $d^4p_1 d^4p_2 d^4p_3 = |J|^4 d^4P d^4q_1 d^4q_2$ .

In general, the Bethe-Salpeter amplitude  $\Psi_A$  can be factorized into the plane wave for center-of-mass motion with total momentum  $P_A$  and an internal wave function that depends only on two relative coordinates  $\xi_1, \xi_2$  describing the motion of internal nucleons/ $\Lambda$  relative to the center of mass.

$$\Psi_A(x_1, x_2, x_3) = (2\pi)^{-4/2} e^{-iP_A \cdot R} \varphi_A(\xi_1, \xi_2). \quad (52)$$

<sup>6</sup>Note that in these calculations, we use bold and italic fonts for three- and four-vectors. For example, the four-vector  $x \equiv (t, \mathbf{r})$  and  $p \equiv (p^0, \mathbf{p})$ . Moreover, the four-vectors product will be indicate with  $p \cdot r \equiv p^0 t - \mathbf{p} \cdot \mathbf{r}$

At this point, Eq. (51) can be rewritten as

$$\begin{aligned} \gamma \frac{dN_A}{d^3P} &= \frac{S_A}{(2\pi)^{20}} |J^{-1}|^4 \int d^4P \int d^4q_1 \int d^4q_2 \int d^4R \int d^4\xi_1 \int d^4\xi_2 \int d^4R' \int d^4\xi'_1 \int d^4\xi'_2 \\ &\quad \times e^{-iP_A \cdot (R-R')} \varphi_A^*(\xi'_1, \xi'_2) \varphi_A(\xi_1, \xi_2) e^{iP \cdot (R-R') + iq_1 \cdot (\xi_1 - \xi'_1) + iq_2 \cdot (\xi_2 - \xi'_2)} \\ &\quad \times W_A \left( p_1, p_2, p_3, \frac{x_1 + x'_1}{2}, \frac{x_2 + x'_2}{2}, \frac{x_3 + x'_3}{2} \right). \end{aligned} \quad (53)$$

Changing variables to the four vectors  $S = (R + R')/2$  and  $T = R - R'$ , we can now integrate over  $T$  since  $x_i + x'_i$ ,  $i = 1, 2, 3$  depends only on  $S$ , obtaining  $(2\pi)^4 \delta^{(4)}(P - P_A)$ . After the integration of this  $\delta$  over  $d^4P$ , we have

$$\begin{aligned} \gamma \frac{dN_A}{d^3P} &= \frac{S_A}{(2\pi)^{16}} |J^{-1}|^4 \int d^4q_1 \int d^4q_2 \int d^4S \int d^4\xi_1 \int d^4\xi_2 \int d^4\xi'_1 \int d^4\xi'_2 \\ &\quad \times \varphi_A^*(\xi'_1, \xi'_2) \varphi_A(\xi_1, \xi_2) e^{iq_1 \cdot (\xi_1 - \xi'_1) + iq_2 \cdot (\xi_2 - \xi'_2)} \\ &\quad \times W_A \left( p_1, p_2, p_3, \frac{x_1 + x'_1}{2}, \frac{x_2 + x'_2}{2}, \frac{x_3 + x'_3}{2} \right) \Big|_{P=P_A}. \end{aligned} \quad (54)$$

For the moment everything is exact. We will now approximate this relation in order to obtain the three-dimensional relation given in Eq. (4). In the following, we introduce the notation  $S = (t_S, \mathbf{S})$ ,  $R = (t_R, \mathbf{R})$ ,  $\xi_i = (\tau_i, \boldsymbol{\xi}_i)$ ,  $i = 1, 2$ , and  $x_i = (t_i, \mathbf{x}_i)$ ,  $i = 1, \dots, 3$ , and similarly for the primed quantities. Clearly  $t_S = (t_R + t'_R)/2$  and  $t_i = t_R +$  linear combination of  $\tau_1$  and  $\tau_2$ . For more details see Ref. [?]

- Low-energy approximation: in the trinucleon rest frame, the particles can be considered as non relativistic, so we can approximate the Bethe-Salpeter amplitude  $\varphi_A(\xi_1, \xi_2)$  with the non relativistic wave function  $\varphi_{NR}(\boldsymbol{\xi}_1, \boldsymbol{\xi}_2)$ . Moreover, in  $W_A$  we can approximate  $p_i^0 \approx c_i P^0$ , disregarding the contribution of the internal energies  $q_1^0$  and  $q_2^0$ . At this point, we can integrate over  $q_1^0$  and  $q_2^0$ :

$$\int \frac{dq_1^0}{2\pi} \frac{dq_2^0}{2\pi} e^{iq_1^0(\tau_1 - \tau'_1) + iq_2^0(\tau_2 - \tau'_2)} = \delta(\tau_1 - \tau'_1) \delta(\tau_2 - \tau'_2) \quad (55)$$

- Equal time approximation: the three particles must exit at the same time from the interaction region in order to form a bound system. Note that in  $W_A$ , the combinations  $(t_i + t'_i)/2$  appear, which can be written as

$$\frac{t_i + t'_i}{2} = \frac{t_R + t'_R}{2} + \dots = t_S + \dots = \tilde{t}_i. \quad (56)$$

In practice, the “time”  $\tilde{t}_i$  are the  $t_i$  where  $t_R$  is replaced by  $t_S$ . We can now assume that  $W_A \sim \delta(\tilde{t}_1 - t_0) \delta(\tilde{t}_2 - t_0) \delta(\tilde{t}_3 - t_0)$ , where  $t_0$  is some “freeze-out” time. We can rewrite this product as

$$\delta(\tilde{t}_1 - t_0) \delta(\tilde{t}_2 - t_0) \delta(\tilde{t}_3 - t_0) = |J| \delta(t_S - t_0) \delta(\tau_1) \delta(\tau_2). \quad (57)$$

This allows for the integration over the time components, obtaining

$$\begin{aligned} \gamma \frac{dN_A}{d^3P} &= \frac{S_A}{(2\pi)^{14}} |J^{-1}|^3 \int d^3q_1 \int d^3q_2 \int d^3S \int d^3\xi_1 \int d^3\xi_2 \int d^3\xi'_1 \int d^3\xi'_2 \\ &\quad \times \varphi_{NR}^*(\boldsymbol{\xi}'_1, \boldsymbol{\xi}'_2) \varphi_{NR}(\boldsymbol{\xi}_1, \boldsymbol{\xi}_2) e^{-iq_1 \cdot (\boldsymbol{\xi}_1 - \boldsymbol{\xi}'_1) - iq_2 \cdot (\boldsymbol{\xi}_2 - \boldsymbol{\xi}'_2)} \\ &\quad \times W_A \left( (c_1 P_d^0, \mathbf{p}_1), (c_2 P_d^0, \mathbf{p}_2), (c_3 P_d^0, \mathbf{p}_3), \frac{(t_0, \mathbf{x}_1 + \mathbf{x}'_1)}{2}, \frac{(t_0, \mathbf{x}_2 + \mathbf{x}'_2)}{2}, \frac{(t_0, \mathbf{x}_3 + \mathbf{x}'_3)}{2} \right) \Big|_{P=P_A}. \end{aligned} \quad (58)$$

$t_0$  can be taken arbitrarily as  $t_0 = 0$ . Reinserting the integration over  $d^3S \times \delta^{(3)}(\mathbf{R} - \mathbf{R}')$ , and going back to the integration over the particle coordinates and momenta, we have

$$\begin{aligned}
\gamma \frac{dN_A}{d^3P} &= \frac{S_A}{(2\pi)^{14}} \int d^3p_1 \int d^3p_2 \int d^3p_3 \int d^3x_1 \int d^3x_2 \int d^3x_3 \int d^3x'_1 \int d^3x'_2 \int d^3x'_3 \\
&\quad \times \Psi_{NR}^*(\mathbf{x}'_1, \mathbf{x}'_2, \mathbf{x}'_3) \Psi_{NR}(\mathbf{x}_1, \mathbf{x}_2, \mathbf{x}_3) e^{-i\mathbf{p}_1 \cdot (\mathbf{x}_1 - \mathbf{x}'_1) - i\mathbf{p}_2 \cdot (\mathbf{x}_2 - \mathbf{x}'_2) - i\mathbf{p}_3 \cdot (\mathbf{x}_3 - \mathbf{x}'_3)} \\
&\quad \times W_A \left( \mathbf{p}_1, \mathbf{p}_2, \mathbf{p}_3, \frac{\mathbf{x}_1 + \mathbf{x}'_1}{2}, \frac{\mathbf{x}_2 + \mathbf{x}'_2}{2}, \frac{\mathbf{x}_3 + \mathbf{x}'_3}{2} \right). \quad (59)
\end{aligned}$$

where  $\Psi_{NR}(\mathbf{x}_1, \mathbf{x}_2, \mathbf{x}_3) = (2\pi)^{-\frac{3}{2}} e^{i\mathbf{P} \cdot \mathbf{R}} \varphi_{NR}(\boldsymbol{\xi}_1, \boldsymbol{\xi}_2)$ . Rescaling  $W_A$  by a factor  $(2\pi)^2$ , the expression above coincides with Eq. (4).

## B HH description of the three-particle wave functions

In this work, the trinucleon bound-state wave functions are calculated using the pair-correlated HH (PHH) method (a variation of the HH method), which has been described many times [37, 59]. The interactions employed are the AV18 NN potential [38], augmented by the UIX 3-body potential [39], and the Minnesota NN potential [40]. The latter interaction is a central potential, but it is able to reproduce the binding energy of  ${}^3\text{He}$  and  ${}^3\text{H}$  within 1%. The convergence of the wave functions and associated observables, as the binding energy, mass radius, etc., is well achieved [37, 59]. Some of these results are given in Table 1.

Model	${}^3\text{H}$		${}^3\text{He}$	
	$B$ (MeV)	$r_p$ (fm)	$B$ (MeV)	$r_p$ (fm)
AV18+UIX	8.479	1.582	7.750	1.771
Minnesota	8.386	1.486	7.711	1.708
Expt.	8.482	1.60	7.718	1.77

Table 1: Binding energies and proton radii of  ${}^3\text{H}$  and  ${}^3\text{He}$  obtained from the employed nuclear interactions.

Regarding hypertriton, we have computed its wave function using the HH method. Since, this application has not reported before, here we give the details of the procedure. In the following, we will specialize to the case where particles 1 and 2 are the nucleons, and particle 3 the  $\Lambda$  hyperon. The Jacobi vectors are then defined as

$$\begin{cases} \boldsymbol{\xi}_2 = \mathbf{r}_2 - \mathbf{r}_1 \\ \boldsymbol{\xi}_1 = \sqrt{\frac{4\kappa}{2+\kappa}} \left( \mathbf{r}_3 - \frac{\mathbf{r}_1 + \mathbf{r}_2}{2} \right), \end{cases} \quad (60)$$

where  $\mathbf{r}_i$  is the position of particle  $i$ ,  $\kappa = m_\Lambda/M$ ,  $M$  being the nucleon mass and  $m_\Lambda$  the mass of the  $\Lambda$  hyperon (in this paper, we disregard the neutron-proton mass difference). The Jacobi coordinates are combined to construct the hyperspherical coordinates, which contain one radial coordinate, the hyperradius  $\rho = (\xi_1^2 + \xi_2^2)^{1/2}$ , and five hyperangles (the four angles describing the directions of  $\boldsymbol{\xi}_1$  and  $\boldsymbol{\xi}_2$  plus  $\varphi = \arctan(\xi_1/\xi_2)$ ), which collectively are denoted as  $\Omega$ .

With these definitions, we have, in the center-of-mass system

$$\frac{\rho^2}{2} = r_1^2 + r_2^2 + \kappa r_3^2 = \frac{2\kappa}{2+\kappa} (r_{31}^2 + r_{32}^2 + \frac{1}{\kappa} r_{12}^2) \quad (61)$$

with  $r_{ij} = |\mathbf{r}_i - \mathbf{r}_j|$  the relative distance between particles  $i$  and  $j$ .

The kinetic energy operator can be written in terms of the hyperspherical coordinates as [37]

$$\begin{aligned}
T &= -\frac{\hbar^2}{2m} \nabla_1^2 - \frac{\hbar^2}{2m} \nabla_2^2 - \frac{\hbar^2}{2M} \nabla_3^2, \\
&= -\frac{\hbar^2}{m} \left[ \frac{d^2}{d\rho^2} + \frac{5}{\rho} \frac{d}{d\rho} - \frac{K^2(\Omega)}{\rho^2} \right], \quad (62)
\end{aligned}$$

where  $K^2(\Omega)$  is the so-called hyperangular operator, depending only on the variables  $\Omega$ . The HH functions are the eigenfunctions of this operator, with eigenvalue

$$K^2(\Omega)\mathcal{Y}_{[K],L,L_z}(\Omega) = K(K+4)\mathcal{Y}_{[K],L,L_z}(\Omega) . \quad (63)$$

Their explicit expression is [37]

$$\mathcal{Y}_{[K],L,L_z}(\Omega) = N_{[K]} \left[ Y_{l_1}(\hat{\xi}_1) Y_{l_2}(\hat{\xi}_2) \right]_{L,L_z} (\cos \varphi)^{l_2} (\sin \varphi)^{l_1} P_{n_2}^{l_1+\frac{1}{2}, l_2+\frac{1}{2}}(\cos 2\varphi) \quad (64)$$

where  $Y_l$  are spherical harmonic functions,  $P_n^{a,b}$  Jacobi polynomials,  $L, L_z$  the total orbital angular momentum and its  $z$  projection,  $N_{[K]}$  a normalization factor, and  $[K] \equiv \{l_1, l_2, n_2\}$ . Finally,  $K$  is the grand angular momentum quantum number, given by  $K = l_1 + l_2 + 2n_2$  ( $l_1, l_2, n_2$  are non-negative integers). The HH functions  $\mathcal{Y}_{[K],L,L_z}(\Omega)$  form a complete and orthonormal set in the five-dimensional  $\Omega$  space.

To construct the hypertriton wave function, we need also to take into account the spin and isospin degrees of freedom. We introduce the basis states

$$\Phi_\mu = \left[ \mathcal{Y}_{[K],L}(\Omega) [(s_1 s_2)_{S_2} s_3]_S \right]_{J,J_z} [t_1 t_2]_{T,T_z} , \quad (65)$$

where  $s_i$  is the spin state of particle  $i$ . The spin states are coupled to a total spin  $S$ , which is coupled to the total orbital angular momentum  $L$  to form the total angular momentum  $J$  of the state we want to describe. The isospin states  $t_1$  and  $t_2$  of the two nucleons are coupled to a total isospin  $T, T_z$  (we remember here that the isospin of the  $\Lambda$  hyperon is zero). Above  $\mu \equiv \{l_1, l_2, n_2, L, S_2, S, T\}$ . Finally, the hypertriton wave function is written as

$$\Psi_{J,J_z} = \sum_{\mu} u_{\mu}(\rho) \Phi_{\mu} \quad (66)$$

where  $u_{\mu}(\rho)$  are functions of the hyperradius to be determined. In order to assure the antisymmetry with respect the exchange of particles 1 and 2 (the two nucleons), the sum over the quantum number  $\mu$  is limited to the values

$$(-)^{l_2+S_2+T} = -1 . \quad (67)$$

The hypertriton is a  $np\Lambda$  state of total angular momentum and parity  $J^\pi = 1/2^+$  and  $T = 0$ . So we have also the additional conditions

$$|L - S| \leq J \leq L + S , \quad (-)^{l_1+l_2} = +1 , \quad T = T_z = 0 . \quad (68)$$

Moreover, the condition to antisymmetrize the two nucleons reduces to  $(-)^{l_2+S_2} = -1$  which means that for the two-nucleons in  $s$ -wave only the spin  $S = 1$  is allowed.

The hyperradial functions  $u_{\mu}(\rho)$  have been expanded in terms of the following functions [37]

$$u_{\mu}(\rho) = \sum_{n=1}^N a_{\mu,n} g_n(\rho) , \quad g_n(\rho) = N_n L_{n-1}^{(5)}(\gamma\rho) e^{-\frac{1}{\rho}\gamma\rho} , \quad (69)$$

Where  $N_n = \gamma^3 \sqrt{n!/(n+5)!}$  are normalization factors and  $\gamma$  a variational parameter. The coefficients  $a_{\mu,n}$  are fixed by means of the Rayleigh-Ritz variational principle, which reads

$$\delta \frac{\langle \Psi_{J,J_z} | H | \Psi_{J,J_z} \rangle}{\langle \Psi_{J,J_z} | \Psi_{J,J_z} \rangle} = 0 , \quad (70)$$

where  $H$  is the Hamiltonian of the system, which we take of the form

$$H = T + V_{NN}(1,2) + V_{N\Lambda}(1,3) + V_{N\Lambda}(2,3) + W_{NN\Lambda}(1,2,3) . \quad (71)$$

Above  $T$  is the kinetic energy operator given in Eq. (62), while  $V_{NN}$  and  $V_{N\Lambda}$  are  $NN$  and  $N\Lambda$  potentials. Finally,  $W_{NN\Lambda}$  is a three-particle potential.

In this paper, we have adopted two versions for these interactions. First of all, we have used a number of simple central interactions of the Gaussian form [43]

$$V_{NN}(1, 2) = \sum_{S=0,1} \bar{V}_S e^{-(r_{12}/\bar{r}_s)^2} \mathcal{P}_{0,S}(1, 2), \quad (72)$$

$$V_{N\Lambda}(1, 3) = \sum_{S=0,1} V_S e^{-(r_{13}/r_s)^2} \mathcal{P}_{0,S}(1, 3), \quad (73)$$

$$W_{NN\Lambda}(1, 2, 3) = W_3 e^{-(r_{13}^2+r_{23}^2)/\rho_3^2}, \quad (74)$$

where  $\mathcal{P}_{0,S}(i, j)$  are projectors on the orbital angular momentum  $\ell = 0$  state and on the spin  $S$  state of particles  $i$  and  $j$ . Clearly  $V_{N\Lambda}(2, 3)$  can be obtained from  $V_{N\Lambda}(1, 3)$  after the substitution  $1 \leftrightarrow 2$ , so in the present study we do not consider charge-symmetry breaking terms in the  $N\Lambda$  interaction. The low-energy Gaussian representation of the  $N\Lambda$  interaction is justified in the context of a leading order effective interaction based on contact interactions, see for example Ref. [60].

The parameters  $\bar{V}_S$  and  $\bar{r}_s$  have been chosen in order to reproduce the experimental  $np$   $s$ -wave scattering lengths and effective ranges. The adopted values are:  $\bar{V}_0 = -30.5459$  MeV,  $\bar{r}_0 = 1.831$  fm,  $\bar{V}_1 = -66.5825$  MeV, and  $\bar{r}_1 = 1.558$  fm. Regarding the  $N\Lambda$  systems, such experimental values are not well known, so the parameters  $V_S$  and  $r_s$  have been fixed to reproduce the  $s$ -wave scattering lengths and effective ranges as calculated by the chiral EFT potentials developed in Refs. [47, 48, 49]. In those references different values of the cutoff have been used to regularize the interaction giving in each case different values of the scattering parameters. Accordingly, for each of them we have extracted different values of  $V_S$  and  $r_s$  [43]. Furthermore, for each of this Gaussian  $V_{N\Lambda}$  we need to include a three-body force, otherwise the hypertriton would be overbound. The corresponding three body parameters  $W_3$  and  $\rho_3$  are then chosen to reproduce the hypertriton binding energy  $B({}_\Lambda^3\text{H}) = 2.40$  MeV [43]. The values of the parameters used in this work are reported in Table 2

Model	1	9
$V_0$ (MeV)	-35.130	-31.851
$r_0$ (fm)	1.375	1.434
$V_1$ (MeV)	-23.239	-42.055
$r_1$ (fm)	1.482	1.126
$W_3$ (MeV)	12.834	11.795
$\rho_3$ (fm)	2.0	2.0

Table 2: The strength  $V_S$  and range  $r_S$  in two spin channels  $S = 0, 1$  of the two Gaussian potentials adopted in this work. These parameters reproduces the  $s$ -wave scattering lengths and effective ranges as calculated by the chiral EFT potentials devised in The last two rows give the strength and range of the three-body force needed to describe the experimental value of  $B({}_\Lambda^3\text{H})$ . The model numbering is taken from Ref. [43].

In addition to the Gaussian interaction, we consider as well the Bodmer-Usmani  $N\Lambda$  interaction [51, 52]

$$V_{N\Lambda}^{BU}(1, 3) = V_C(r_{13})(1 - \epsilon + \epsilon P_x) + 0.25 V_G T_\pi^2(r_{13}) \sigma_1 \cdot \sigma_3, \quad T_\pi(r) = \left(1 + \frac{3}{\mu r} \frac{3}{(\mu r)^2}\right) \frac{e^{-\mu r}}{\mu r} \left(1 - e^{-c_\pi r^2}\right)^3 \quad (75)$$

with  $P_x$  the space-exchange operator. The  $r$ -dependence of the potentials has the form  $V_C(r) = W_C / (1 + e^{(r-\bar{r})/a}) - \bar{v} T_\pi^2(r)$  where  $T_\pi(r)$  is the pion exchange tensor potential. The values of the parameters used in the present study are:  $\epsilon = 0$ ,  $\bar{r} = 0.5$  fm,  $a = 0.2$  fm,  $\bar{v} = 6.20$  MeV,  $V_G = 0.25$  MeV,  $W_C = 2137$  MeV,  $\mu = 0.69953$  fm $^{-1}$ , and  $c_\pi = 2.1$  fm $^{-2}$ . Associated with this potential we have used the following three-body force

$$W_{NN\Lambda}^{BU}(1, 2, 3) = W_3^{BU} T_\pi^2(r_{13}) T_\pi^2(r_{23}) \quad (76)$$

with the value  $W_3^{BU} = 0.025$  MeV in order to reproduce the hypertriton binding energy.

Once the interaction is chosen, standard numerical methods allow for the evaluation of the matrix elements  $H_{\mu,n,\mu',n'} = \langle g_n(\rho) \Phi_\mu | H | g_{n'}(\rho) \Phi_{\mu'} \rangle$ , while  $\langle g_n(\rho) \Phi_\mu | g_{n'}(\rho) \Phi_{\mu'} \rangle = \delta_{n,n'} \delta_{\mu,\mu'}$  since  $\Phi_\mu$  and

$g_n(\rho)$  are orthonormal sets. The application of the Rayleigh-Ritz variational principle therefore reduces to a standard eigenvalue problem

$$\sum_{\mu', n'} H_{\mu, n, \mu', n'} a_{\mu', n'} = E a_{\mu, n} . \quad (77)$$

Note that for a central Gaussian potential, it is sufficient to include in the expansion basis only states  $\Phi_\mu$  with  $L = 0$  and  $S = 1/2$ . In Table 3, we show examples of convergence. In the considered cases, we have included in the expansion basis all the states  $\Phi_\mu$  with quantum numbers  $L = 0$  and  $S = 1/2$  and  $l_1 + l_2 + n_2 \leq K$  (and compatible with the conditions given in Eqs. (67–68)). Then, the convergence is studied by increasing the values of  $K$  and  $N$ , the latter being the number of expansion states of the hyperradial functions.

$K$	$N$	$N_{HH}$	Model 1	Model 9	BU
20	24	66	-2.267	-2.268	-2.221
30	24	136	-2.340	-2.340	-2.351
40	24	231	-2.366	-2.366	-2.398
50	24	351	-2.376	-2.376	-2.402
60	24	496	-2.380	-2.380	-2.407
60	28	496	-2.380	-2.380	-2.408

Table 3: Convergence of the hypertriton energy as function of the maximum  $K$  of HH functions  $\Phi_\mu$  and number of functions  $g_n$  used to expand the hyperradial functions for the various interactions used in this work. Above  $N_{HH}$  is the total number of HH states included in the expansion basis for each  $K$  value. Here we have performed the calculation for  $\gamma = 2.8 \text{ fm}^{-1}$ . In all the cases, the Hamiltonian includes the  $NN\Lambda$  interaction.

As it can be seen by inspecting Table 3, the convergence is well achieved for values of  $K$  around 50-60. Values of the parameter  $N$  around 24-28 are sufficient to have an accurate description of the hyperradial functions  $u_\mu(\rho)$ , see Eq. (69). In conclusion, the HH method furnishes accurate description of the hypertriton for the adopted potential models.

## C Congleton Formalism for Hypertriton

For the Congleton formalism, we use the Jacobi coordinate transformation given, and the total position space wave function is given as where  $\Psi_{\Lambda^3\text{H}}$  and  $\Psi_i$  for  $i = 1, 2, 3$  are the wave functions for  ${}^3_\Lambda\text{H}$  and nucleons.  $\Psi_{\Lambda^3\text{H}}$  is assumed to be factorized into the plane wave for COM motion and an internal wave function that depends only on two relative coordinates.

$$\Psi_{\Lambda^3\text{H}}(\mathbf{x}_1, \mathbf{x}_2, \mathbf{x}_3) = (2\pi)^{-3/2} e^{i\mathbf{P}_{\Lambda^3\text{H}} \cdot \mathbf{R}} \varphi_{\Lambda^3\text{H}}(\boldsymbol{\xi}_1, \boldsymbol{\xi}_2) \quad (78)$$

Where relative Jacobi coordinates are defined in terms of the mass of two identical masses  $m_1 = m_2 = M$  for proton and neutron and a third particle,  $\Lambda$  with a different mass  $m_3$ . We define the mass ratio as  $\kappa = \frac{m_3}{M}$

$$J^{-1} = \begin{pmatrix} 0 & \frac{1}{2} & -\frac{1}{2} \\ \frac{2}{2+\kappa} & -\frac{\kappa}{2+\kappa} & -\frac{\kappa}{2+\kappa} \\ \frac{\kappa}{2+\kappa} & \frac{\kappa}{2+\kappa} & \frac{2}{2+\kappa} \end{pmatrix} \quad (79)$$

$$\begin{pmatrix} \boldsymbol{\xi}_1 \\ \boldsymbol{\xi}_2 \\ \mathbf{R} \end{pmatrix} = J \times \begin{pmatrix} \mathbf{x}_1 \\ \mathbf{x}_2 \\ \mathbf{x}_3 \end{pmatrix} \quad (80)$$

with  $|J| = -\frac{(2+\kappa)^2}{2+\kappa^2}$

$$\begin{aligned} \mathbf{x}_1 &= \frac{\kappa \mathbf{R}}{2+\kappa} + \frac{2\xi_2}{2+\kappa}, & \mathbf{x}'_1 &= \frac{\kappa \mathbf{R}'}{2+\kappa} + \frac{2\xi'_2}{2+\kappa}, \\ \mathbf{x}_2 &= \frac{\mathbf{R}}{2+\kappa} + \frac{\xi_1}{2} - \frac{\kappa \xi_2}{2+\kappa}, & \mathbf{x}'_2 &= \frac{\mathbf{R}'}{2+\kappa} + \frac{\xi'_1}{2} - \frac{\kappa \xi'_2}{2+\kappa}, \\ \mathbf{x}_3 &= \frac{\mathbf{R}}{2+\kappa} - \frac{\xi_1}{2} - \frac{\kappa \xi_2}{2+\kappa}, & \mathbf{x}'_3 &= \frac{\mathbf{R}'}{2+\kappa} - \frac{\xi'_1}{2} - \frac{\kappa \xi'_2}{2+\kappa}, \end{aligned} \quad (81)$$

with momentum conjugates

$$\begin{pmatrix} \mathbf{q}_1 \\ \mathbf{q}_2 \\ \mathbf{P} \end{pmatrix} = J^{-1} \times \begin{pmatrix} \mathbf{p}_1 \\ \mathbf{p}_2 \\ \mathbf{p}_3 \end{pmatrix} \quad (82)$$

and

$$\begin{aligned} \mathbf{p}_1 &= \frac{\kappa(2+\kappa)\mathbf{P}}{2+\kappa^2} + \frac{(2+\kappa)\mathbf{q}_2}{2+\kappa^2} \\ \mathbf{p}_2 &= \frac{(2+\kappa)\mathbf{P}}{2+\kappa^2} + \mathbf{q}_1 - \frac{\kappa(2+\kappa)\mathbf{q}_2}{2(2+\kappa^2)}, \\ \mathbf{p}_3 &= \frac{(2+\kappa)\mathbf{P}}{2+\kappa^2} - \mathbf{q}_1 - \frac{\kappa(2+\kappa)\mathbf{q}_2}{2(2+\kappa^2)}, \end{aligned} \quad (83)$$

satisfying the condition,  $\mathbf{p}_1 \cdot \mathbf{x}_1 + \mathbf{p}_2 \cdot \mathbf{x}_2 + \mathbf{p}_3 \cdot \mathbf{x}_3 = \xi_1 \cdot \mathbf{q}_1 + \xi_2 \cdot \mathbf{q}_2 + \mathbf{R} \cdot \mathbf{P}$ . Finally defining  $\mathbf{R} = \frac{\xi_1 + \xi_2}{2}$  and  $\mathbf{R}' = \frac{\xi_2 - \xi_1}{2}$  as well as  $d^3x_1 d^3x_2 d^3x_3 d^3x'_1 d^3x'_2 d^3x'_3 = \frac{|J^{-1}|^6}{8} d^3\xi_1 d^3\xi_2 d^3\xi'_1 d^3\xi'_2 d^3\xi_1 d^3\xi_2$  with  $d^3R d^3R' = \frac{1}{8} d^3\xi_1 d^3\xi_2$ . We obtain the yield in terms of the Jacobi coordinates and the Hypertriton wave function as

$$\begin{aligned} \frac{dN_{\Lambda\text{H}}}{d^3P} &= \frac{S_{\Lambda\text{H}}^3}{(2\pi)^{12}} \left( \frac{|J^{-1}|}{2} \right)^3 \int d^3\xi_1 d^3\xi_2 d^3\xi'_1 d^3\xi'_2 d^3\xi_1 d^3\xi_2 d^3q_1 d^3q_2 d^3P e^{i\xi_1 \cdot (\mathbf{P} - \mathbf{P}_{\Lambda\text{H}}^3)} e^{-\frac{(2+\kappa^2)\xi_2^2}{8\sigma^2(2+\kappa)^2}} \\ &\times \varphi_{\Lambda\text{H}}^3(\xi_1, \xi_2) \varphi_{\Lambda\text{H}}^*(\xi'_1, \xi'_2) e^{i(\mathbf{q}_1 \cdot \xi_1 - \mathbf{q}_1 \cdot \xi'_1 + \mathbf{q}_2 \cdot \xi_2 - \mathbf{q}_2 \cdot \xi'_2)} \times (2\pi\sigma^2)^{-9/2} e^{\chi^2} G_{\text{np}\Lambda}(\mathbf{p}_1, \mathbf{p}_2, \mathbf{p}_3)|_{\mathbf{P}=\mathbf{P}_{\Lambda\text{H}}^3} \end{aligned} \quad (84)$$

with a substitution of defined in terms of  $\chi^2 = -\frac{4((\xi_1 + \xi'_1)^2 + 2(\xi_2 + \xi'_2)^2) + 4\kappa(\xi_1 + \xi'_1)^2 + \kappa^2(\xi_1^2 + \xi'_1^2 \cdot (2\xi_1 + \xi'_1) + 4\xi_2^2 + 4\xi'_2 \cdot (2\xi_2 + \xi'_2))}{16\sigma^2(2+\kappa)^2}$ .

Performing pure  $\delta$  integral  $\int d^3\xi_1 e^{i(\mathbf{P} - \mathbf{P}_{\Lambda\text{H}}^3) \cdot \xi_1} = (2\pi)^3 \delta(\mathbf{P} - \mathbf{P}_{\Lambda\text{H}}^3)$  and  $\int d^3P$  and  $\int d^3\xi_2$  in Eq. 84

$$\begin{aligned} \frac{dN_{\Lambda\text{H}}}{d^3P} &= \frac{S_{\Lambda\text{H}}^3}{(2\pi)^9 (2\pi\sigma^2)^{9/2}} \frac{8\sqrt{2}\pi^{3/2} |J^{-1}|^3 \sigma^3 (2+\kappa)^3}{(2+\kappa^2)^{3/2}} \int d^3\xi_1 d^3\xi_2 d^3\xi'_1 d^3\xi'_2 d^3q_1 d^3q_2 \varphi_{\Lambda\text{H}}^3(\xi_1, \xi_2) \varphi_{\Lambda\text{H}}^*(\xi'_1, \xi'_2) \\ &\times e^{i(\mathbf{q}_1 \cdot (\xi_1 - \xi'_1) + \mathbf{q}_2 \cdot (\xi_2 - \xi'_2))} \times e^{\chi^2} G_{\text{np}\Lambda}(\mathbf{p}_1, \mathbf{p}_2, \mathbf{p}_3)|_{\mathbf{P}=\mathbf{P}_{\Lambda\text{H}}^3} \end{aligned} \quad (85)$$

Further simplifications are made by making the following coordinate transformations  $\xi_1 = \mathbf{r}_1 + \zeta_1/2$ ,  $\xi'_1 = \mathbf{r}_1 - \zeta_1/2$ , and  $\xi_2 = \mathbf{r}_2 + \zeta_2/2$ ,  $\xi'_2 = \mathbf{r}_2 - \zeta_2/2$ , with  $d^3\xi_1 d^3\xi_2 d^3\xi'_1 d^3\xi'_2 = d^3r_1 d^3r_2 d^3\zeta_1 d^3\zeta_2$ .

$$\begin{aligned} \frac{dN_{\Lambda\text{H}}}{d^3P} &= \frac{S_{\Lambda\text{H}}^3}{(2\pi)^9 (2\pi\sigma^2)^{9/2}} \frac{8\sqrt{2}\pi^{3/2} |J^{-1}|^3 \sigma^3 (2+\kappa)^3}{(2+\kappa^2)^{3/2}} \int d^3r_1 d^3r_2 d^3\zeta_1 d^3\zeta_2 d^3q_1 d^3q_2 \\ &\times \varphi_{\Lambda\text{H}}^3(\mathbf{r}_1 + \frac{\zeta_1}{2}, \mathbf{r}_2 + \frac{\zeta_2}{2}) \varphi_{\Lambda\text{H}}^*(\mathbf{r}_1 - \frac{\zeta_1}{2}, \mathbf{r}_2 - \frac{\zeta_2}{2}) e^{i(\mathbf{q}_1 \cdot \zeta_1 + \mathbf{q}_2 \cdot \zeta_2)} e^{-\frac{r_1^2(2\kappa+1)^2 + 4r_2^2(2+\kappa^2)}{4\sigma^2(2+\kappa)^2}} G_{\text{np}\Lambda}(\mathbf{p}_1, \mathbf{p}_2, \mathbf{p}_3)|_{\mathbf{P}=\mathbf{P}_{\Lambda\text{H}}^3} \end{aligned} \quad (86)$$

Where

$$\mathcal{D}(\mathbf{q}_1, \mathbf{q}_2, \mathbf{r}_1, \mathbf{r}_2) = \int d^3\zeta_1 \int d^3\zeta_2 \varphi_{\Lambda\text{H}}^3(\mathbf{r}_1 + \frac{\zeta_1}{2}, \mathbf{r}_2 + \frac{\zeta_2}{2}) \varphi_{\Lambda\text{H}}^*(\mathbf{r}_1 - \frac{\zeta_1}{2}, \mathbf{r}_2 - \frac{\zeta_2}{2}) e^{i(\mathbf{q}_1 \cdot \zeta_1 + \mathbf{q}_2 \cdot \zeta_2)} \quad (87)$$

Within the approach developed by Congleton et al [41], the wave function  $\varphi_{\Lambda\text{H}}^3$  is defined as the product of  $\Lambda$ -d wave function and deuteron wave function, assuming deuteron is undisturbed bound object at the core.

$$\varphi_{\Lambda\text{H}}^3 = \varphi_{\Lambda}\varphi_d. \quad (88)$$

The Wigner density can be written as the product of the Wigner densities for the  $\Lambda$  and deuteron as follows:

$$\begin{aligned} \mathcal{D}(\mathbf{q}_1, \mathbf{q}_2, \mathbf{r}_1, \mathbf{r}_2) &= \int d^3\zeta_1 \int d^3\zeta_2 \varphi_{\Lambda}(\mathbf{r}_1 + \frac{\zeta_1}{2})\varphi_{\Lambda}^*(\mathbf{r}_1 - \frac{\zeta_1}{2}), \varphi_d(\mathbf{r}_2 + \frac{\zeta_2}{2})\varphi_d^*(\mathbf{r}_2 - \frac{\zeta_2}{2}) e^{i(\mathbf{q}_1 \cdot \zeta_1 + \mathbf{q}_2 \cdot \zeta_2)} \\ &= \int d^3\zeta_1 \varphi_{\Lambda}(\mathbf{r}_1 + \frac{\zeta_1}{2})\varphi_{\Lambda}^*(\mathbf{r}_1 - \frac{\zeta_1}{2}) e^{i\mathbf{q}_1 \cdot \zeta_1} \int d^3\zeta_2 \varphi_d(\mathbf{r}_2 + \frac{\zeta_2}{2})\varphi_d^*(\mathbf{r}_2 - \frac{\zeta_2}{2}) e^{i\mathbf{q}_2 \cdot \zeta_2} \\ &= \mathcal{D}_{\Lambda}(\mathbf{q}_1, \mathbf{r}_1)\mathcal{D}_d(\mathbf{q}_2, \mathbf{r}_2) \end{aligned} \quad (89)$$

Where, the Wigner densities  $\mathcal{D}_d(\mathbf{k}_2, \mathbf{r}_2)$ , is computed in coordinate space. The computation of  $\mathcal{D}_d(\mathbf{k}_2, \mathbf{r}_2)$  has already been provided in a previous work [27], using the Argonne  $v_{18}$  wave function. While  $\mathcal{D}_{\Lambda}(\mathbf{q}_1, \mathbf{r}_1)$  can be easily computed using the momentum-space wave function by the Congleton approach

$$\varphi_{\Lambda}(q) = N(Q) \frac{e^{-\left(\frac{q}{Q}\right)^2}}{q^2 + \alpha^2}, \quad (90)$$

with a normalization function

$$N(Q) = \left\{ \frac{\pi}{4\alpha} \left[ \left( \frac{4\alpha^2}{Q^2} + 1 \right) \text{Cerfe} \left( \frac{\sqrt{2}\alpha}{Q} \right) - \frac{2\alpha \left( \frac{2}{\pi} \right)^{1/2}}{Q} \right] \right\}^{-1/2} \quad (91)$$

For  $\alpha = 0.068 \text{ fm}^{-1}$   $N^2(2.5 \text{ fm}^{-1}) = 0.094$  and  $\int |\phi_{\Lambda}(q)|^2 d^3q = 4\pi$ . Finally, the Wigner density of the hypertriton  $\Lambda$  part is given by

$$\mathcal{D}_{\Lambda}(\mathbf{q}, \mathbf{r}) = N(Q)^2 \int_0^{\infty} dk \frac{4i\pi (-1 + e^{2ikr})}{qr(k^2 + 4(\alpha^2 + q^2))} \log \left( \frac{4\alpha^2 + (k - 2q)^2}{4\alpha^2 + (k + 2q)^2} \right) e^{-\frac{k^2 + 2ikQ^2r + 4q^2}{2Q^2}} \quad (92)$$

and  $\mathcal{D}_{\Lambda}(0, 0)/4\pi = 8.0$  as expected. The probability is given as

$$\begin{aligned} \mathcal{P}(q_1, q_2, \sigma) &= \frac{S_{\Lambda\text{H}}^3}{(2\pi)^3 \sigma^6} |J|^{-3} \frac{(2 + \kappa)^3}{(2 + \kappa^2)^{3/2}} \int d^3r_1 \int d^3r_2 \mathcal{D}_{\Lambda}(\mathbf{q}_1, \mathbf{r}_1)\mathcal{D}_d(\mathbf{q}_2, \mathbf{r}_2) e^{-\frac{r_1^2(2+\kappa)^2 + 4r_2^2(2+\kappa^2)}{4\sigma^2(2+\kappa)^2}} \\ &= \frac{(2 + \kappa^2)^{3/2}}{(2 + \kappa)^3} \times \frac{S_{\Lambda\text{H}}^3}{(2\pi)^3 \sigma^6} \int d^3r_1 \int d^3r_2 \mathcal{D}_{\Lambda}(\mathbf{q}_1, \mathbf{r}_1)\mathcal{D}_d(\mathbf{q}_2, \mathbf{r}_2) e^{-\frac{r_1^2(2+\kappa)^2 + 4r_2^2(2+\kappa^2)}{4\sigma^2(2+\kappa)^2}} \end{aligned} \quad (93)$$

with  $\int d^3q_1 d^3q_2 \frac{|J|^3}{(2\pi)^9} G_{\text{np}\Lambda}(\mathbf{p}_1, \mathbf{p}_2, \mathbf{p}_3)|_{\mathbf{P}=\mathbf{P}_{\Lambda\text{H}}} = 1$ .

## References

- [1] M. A. Lisa, S. Pratt, R. Soltz, and U. Wiedemann, ‘‘Femtосcopy in relativistic heavy ion collisions,’’ *Ann. Rev. Nucl. Part. Sci.* **55** (2005) 357–402, [arXiv:nucl-ex/0505014](#).
- [2] L. Fabbietti, V. Mantovani Sarti, and O. Vazquez Doce, ‘‘Study of the Strong Interaction Among Hadrons with Correlations at the LHC,’’ *Ann. Rev. Nucl. Part. Sci.* **71** (2021) 377–402, [arXiv:2012.09806 \[nucl-ex\]](#).
- [3] **ALICE** Collaboration, S. Acharya *et al.*, ‘‘Multiplicity dependence of (anti-)deuteron production in pp collisions at  $\sqrt{s} = 7 \text{ TeV}$ ,’’ *Phys. Lett. B* **794** (2019) 50–63, [arXiv:1902.09290 \[nucl-ex\]](#).
- [4] **ALICE** Collaboration, S. Acharya *et al.*, ‘‘Multiplicity dependence of light (anti-)nuclei production in p-Pb collisions at  $\sqrt{s_{\text{NN}}} = 5.02 \text{ TeV}$ ,’’ *Phys. Lett. B* **800** (2020) 135043, [arXiv:1906.03136 \[nucl-ex\]](#).

- [5] **ALICE** Collaboration, S. Acharya *et al.*, “Production of light (anti)nuclei in pp collisions at  $\sqrt{s} = 5.02$  TeV,” *Eur. Phys. J. C* **82** no. 4, (2022) 289, [arXiv:2112.00610 \[nucl-ex\]](#).
- [6] **ALICE** Collaboration, S. Acharya *et al.*, “Production of light (anti)nuclei in pp collisions at  $\sqrt{s} = 13$  TeV,” *JHEP* **01** (2022) 106, [arXiv:2109.13026 \[nucl-ex\]](#).
- [7] **ALICE** Collaboration, S. Acharya *et al.*, “Light (anti)nuclei production in Pb-Pb collisions at  $\sqrt{s_{NN}}=5.02$  TeV,” *Phys. Rev. C* **107** no. 6, (2023) 064904, [arXiv:2211.14015 \[nucl-ex\]](#).
- [8] **ALICE** Collaboration, S. Acharya *et al.*, “Search for a common baryon source in high-multiplicity pp collisions at the LHC,” *Phys. Lett. B* **811** (2020) 135849, [arXiv:2004.08018 \[nucl-ex\]](#).
- [9] **ALICE** Collaboration, S. Acharya *et al.*, “Common femtoscopic hadron-emission source in pp collisions at the LHC,” *Eur. Phys. J. C* **85** no. 2, (2025) 198, [arXiv:2311.14527 \[hep-ph\]](#).
- [10] **ALICE** Collaboration, B. Abelev *et al.*, “Charged kaon femtoscopic correlations in pp collisions at  $\sqrt{s} = 7$  TeV,” *Phys. Rev. D* **87** no. 5, (2013) 052016, [arXiv:1212.5958 \[hep-ex\]](#).
- [11] **ALICE** Collaboration, J. Adam *et al.*, “One-dimensional pion, kaon, and proton femtoscopy in Pb-Pb collisions at  $\sqrt{s_{NN}}=2.76$  TeV,” *Phys. Rev. C* **92** no. 5, (2015) 054908, [arXiv:1506.07884 \[nucl-ex\]](#).
- [12] **ALICE** Collaboration, S. Acharya *et al.*, “Exploring the Strong Interaction of Three-Body Systems at the LHC,” *Phys. Rev. X* **14** no. 3, (2024) 031051, [arXiv:2308.16120 \[nucl-ex\]](#).
- [13] A. Andronic, P. Braun-Munzinger, J. Stachel, and H. Stoecker, “Production of light nuclei, hypernuclei and their antiparticles in relativistic nuclear collisions,” *Phys. Lett. B* **697** (2011) 203–207, [arXiv:1010.2995 \[nucl-th\]](#).
- [14] A. Andronic, P. Braun-Munzinger, K. Redlich, and J. Stachel, “Decoding the phase structure of QCD via particle production at high energy,” *Nature* **561** no. 7723, (2018) 321–330, [arXiv:1710.09425 \[nucl-th\]](#).
- [15] V. Vovchenko, B. Dönigus, and H. Stoecker, “Multiplicity dependence of light nuclei production at LHC energies in the canonical statistical model,” *Phys. Lett. B* **785** (2018) 171–174, [arXiv:1808.05245 \[hep-ph\]](#).
- [16] S. T. Butler and C. A. Pearson, “Deuterons from High-Energy Proton Bombardment of Matter,” *Phys. Rev.* **129** (1963) 836–842.
- [17] L. P. Csernai and J. I. Kapusta, “Entropy and Cluster Production in Nuclear Collisions,” *Phys. Rept.* **131** (1986) 223–318.
- [18] J. L. Nagle, B. S. Kumar, D. Kusnezov, H. Sorge, and R. Mattiello, “Coalescence of deuterons in relativistic heavy ion collisions,” *Phys. Rev. C* **53** (1996) 367–376.
- [19] R. Scheibl and U. W. Heinz, “Coalescence and flow in ultrarelativistic heavy ion collisions,” *Phys. Rev. C* **59** (1999) 1585–1602, [arXiv:nucl-th/9809092](#).
- [20] K. Blum and M. Takimoto, “Nuclear coalescence from correlation functions,” *Phys. Rev. C* **99** no. 4, (2019) 044913, [arXiv:1901.07088 \[nucl-th\]](#).
- [21] **A Large Ion Collider Experiment, ALICE** Collaboration, S. Acharya *et al.*, “Hypertriton Production in p-Pb Collisions at  $\sqrt{s_{NN}}=5.02$  TeV,” *Phys. Rev. Lett.* **128** no. 25, (2022) 252003, [arXiv:2107.10627 \[nucl-ex\]](#).
- [22] J. Steinheimer, K. Gudima, A. Botvina, I. Mishustin, M. Bleicher, and H. Stoecker, “Hypernuclei, dibaryon and antinuclei production in high energy heavy ion collisions: Thermal production versus Coalescence,” *Phys. Lett. B* **714** (2012) 85–91, [arXiv:1203.2547 \[nucl-th\]](#).
- [23] F. Bellini and A. P. Kalweit, “Testing production scenarios for (anti-)(hyper-)nuclei and exotica at energies available at the CERN Large Hadron Collider,” *Phys. Rev. C* **99** no. 5, (2019) 054905, [arXiv:1807.05894 \[hep-ph\]](#).

- [24] F. Bellini, K. Blum, A. P. Kalweit, and M. Puccio, “Examination of coalescence as the origin of nuclei in hadronic collisions,” *Physical Review C* **103** no. 1, (Jan., 2021) .  
<http://dx.doi.org/10.1103/PhysRevC.103.014907>.
- [25] **ALICE** Collaboration, S. Acharya *et al.*, “Measurement of the Lifetime and  $\Lambda$  Separation Energy of  $\text{HA3}$ ,” *Phys. Rev. Lett.* **131** no. 10, (2023) 102302, [arXiv:2209.07360](https://arxiv.org/abs/2209.07360) [[nucl-ex](#)].
- [26] M. Kachelrieß, S. Ostapchenko, and J. Tjemsland, “Alternative coalescence model for deuteron, tritium, helium-3 and their antinuclei,” *The European Physical Journal A* **56** no. 1, (Jan., 2020) .  
<http://dx.doi.org/10.1140/epja/s10050-019-00007-9>.
- [27] M. Mahlein, L. Barioglio, F. Bellini, L. Fabbietti, C. Pinto, B. Singh, and S. Tripathy, “A realistic coalescence model for deuteron production,” *Eur. Phys. J. C* **83** no. 9, (2023) 804, [arXiv:2302.12696](https://arxiv.org/abs/2302.12696) [[hep-ex](#)].
- [28] F. Donato, N. Fornengo, and P. Salati, “Anti-deuterons as a signature of supersymmetric dark matter,” *Phys. Rev.* **D62** (2000) 043003, [arXiv:hep-ph/9904481](https://arxiv.org/abs/hep-ph/9904481) [[hep-ph](#)].
- [29] A. Ibarra and S. Wild, “Prospects of antideuteron detection from dark matter annihilations or decays at AMS-02 and GAPS,” *JCAP* **02** (2013) 021, [arXiv:1209.5539](https://arxiv.org/abs/1209.5539) [[hep-ph](#)].
- [30] M. Cirelli *et al.*, “Anti-helium from Dark Matter annihilations,” *JHEP* **08** (2014) 009.
- [31] E. Carlson, A. Coogan, T. Linden, S. Profumo, A. Ibarra, and S. Wild, “Antihelium from Dark Matter,” *Phys. Rev. D* **89** no. 7, (2014) 076005, [arXiv:1401.2461](https://arxiv.org/abs/1401.2461) [[hep-ph](#)].
- [32] M. Korsmeier, F. Donato, and N. Fornengo, “Prospects to verify a possible dark matter hint in cosmic antiprotons with antideuterons and antihelium,” *Phys. Rev. D* **97** no. 10, (2018) 103011, [arXiv:1711.08465](https://arxiv.org/abs/1711.08465) [[astro-ph.HE](#)].
- [33] K. Blum, K. C. Y. Ng, R. Sato, and M. Takimoto, “Cosmic rays, antihelium, and an old navy spotlight,” *Phys. Rev. D* **96** no. 10, (2017) 103021, [arXiv:1704.05431](https://arxiv.org/abs/1704.05431) [[astro-ph.HE](#)].
- [34] P. von Doetinchem *et al.*, “Cosmic-ray antinuclei as messengers of new physics: status and outlook for the new decade,” *JCAP* **08** (2020) 035.
- [35] S. Acharya *et al.*, “Measurement of anti- $^3\text{He}$  nuclei absorption in matter and impact on their propagation in the Galaxy,” *Nature Phys* **19** no. 1, (2023) 61–71.
- [36] M. Mahlein, C. Pinto, and L. Fabbietti, “ToMCCA: a Toy Monte Carlo Coalescence Afterburner,” *Eur. Phys. J. C* **84** no. 11, (2024) 1136, [arXiv:2404.03352](https://arxiv.org/abs/2404.03352) [[hep-ph](#)].
- [37] A. Kievsky, S. Rosati, M. Viviani, L. Marcucci, and L. Girlanda, “A High-precision variational approach to three- and four-nucleon bound and zero-energy scattering states,” *J. Phys. G* **35** (2008) 063101, [arXiv:0805.4688](https://arxiv.org/abs/0805.4688) [[nucl-th](#)].
- [38] R. B. Wiringa, V. G. J. Stoks, and R. Schiavilla, “An Accurate nucleon-nucleon potential with charge independence breaking,” *Phys. Rev. C* **51** (1995) 38–51, [arXiv:nucl-th/9408016](https://arxiv.org/abs/nucl-th/9408016).
- [39] B. S. Pudliner, V. R. Pandharipande, J. Carlson, and R. B. Wiringa, “Quantum Monte Carlo calculations of  $A \leq 6$  nuclei,” *Phys. Rev. Lett.* **74** (1995) 4396–4399, [arXiv:nucl-th/9502031](https://arxiv.org/abs/nucl-th/9502031).
- [40] D. R. Thompson *et al.*, “Systematic investigation of scattering problems with the resonating-group method,” *Nucl. Phys. A* **286** no. 1, (Aug., 1977) 53–66.
- [41] J. G. Gongleton, “A simple model of the hypertriton,” *Journal of Physics G: Nuclear and Particle Physics* **18** no. 2, (Feb, 1992) 339.  
<https://dx.doi.org/10.1088/0954-3899/18/2/015>.
- [42] F. Hildenbrand *et al.*, “Three-body hypernuclei in pionless effective field theory,” *Phys. Rev. C* **100** no. 3, (Sept., 2019) 034002.

- [43] E. Garrido, A. Kievsky, M. Gattobigio, M. Viviani, L. E. Marcucci, R. Del Grande, L. Fabbietti, and D. Melnichenko, “ $p\Lambda$  and  $pp\Lambda$  correlation functions,” *Phys. Rev. C* **110** no. 5, (2024) 054004, [arXiv:2408.01750](https://arxiv.org/abs/2408.01750) [nucl-th].
- [44] L. E. Marcucci, J. Dohet-Eraly, L. Girlanda, A. Gnech, A. Kievsky, and M. Viviani, “The hyperspherical harmonics method: A tool for testing and improving nuclear interaction models,” *Front. in Phys.* **8** (2020) 69, [arXiv:1912.09751](https://arxiv.org/abs/1912.09751) [nucl-th]. <https://www.frontiersin.org/article/10.3389/fphy.2020.00069>.
- [45] S. Acharya *et al.*, “Search for a common baryon source in high-multiplicity pp collisions at the LHC,” *Phys. Lett. B* **811** (Dec., 2020) 135849.
- [46] ALICE Collaboration, “Investigating the  $p\text{-}\pi^\pm$  and  $p\text{-}p\text{-}\pi^\pm$  dynamics with femtoscopy in pp collisions at  $\sqrt{s} = 13$  TeV,” (2025) . <https://arxiv.org/abs/2502.20200>.
- [47] S. Petschauer, J. Haidenbauer, N. Kaiser, U.-G. Meißner, and W. Weise, “Hyperon-nuclear interactions from SU(3) chiral effective field theory,” *Front. in Phys.* **8** (2020) 12, [arXiv:2002.00424](https://arxiv.org/abs/2002.00424) [nucl-th].
- [48] J. Haidenbauer, A. Nogga, and I. Vidaña, “Predictions for charmed nuclei based on  $Y_cN$  forces inferred from lattice QCD simulations,” *Eur. Phys. J. A* **56** no. 7, (2020) 195, [arXiv:2003.07768](https://arxiv.org/abs/2003.07768) [nucl-th].
- [49] J. Haidenbauer, U.-G. Meißner, A. Nogga, and H. Le, “Hyperon–nucleon interaction in chiral effective field theory at next-to-next-to-leading order,” *Eur. Phys. J. A* **59** no. 3, (2023) 63, [arXiv:2301.00722](https://arxiv.org/abs/2301.00722) [nucl-th].
- [50] D. L. Mihaylov *et al.*, “Constraining the  $p\{\Lambda\}$  interaction from a combined analysis of scattering data and correlation functions,” *arXiv* (Dec., 2023) , 2312.16970.
- [51] A. R. Bodmer, Q. N. Usmani, and J. Carlson, “Binding energies of hypernuclei and three-body ANN forces,” *Phys. Rev. C* **29** (1984) 684–687.
- [52] A. R. Bodmer and Q. N. Usmani, “Binding Energies of the S Shell Hypernuclei and the  $\Lambda$  Well Depth,” *Nucl. Phys. A* **477** (1988) 621–651.
- [53] F. Bellini, K. Blum, A. P. Kalweit, and M. Puccio, “Examination of coalescence as the origin of nuclei in hadronic collisions,” *Phys. Rev. C* **103** (Jan, 2021) 014907. <https://link.aps.org/doi/10.1103/PhysRevC.103.014907>.
- [54] K. Redlich *et al.*, “Exact strangeness conservation in heavy ion collisions,” *EPJ Web Conf* **259** (2022) .
- [55] D. Ruggiano, “Two-particle angular correlations of identified particles in pp collisions at  $\sqrt{s} = 13$  TeV with ALICE,” *arXiv* (Nov., 2023) , 2311.09833.
- [56] S. Acharya *et al.*, “Production of light (anti)nuclei in pp collisions at  $\sqrt{s} = 13$  TeV,” *JHEP* **01** (2022) 106.
- [57] ALICE Collaboration, S. Acharya *et al.*, “Multiplicity dependence of charged-particle production in pp, p-Pb, Xe-Xe and Pb-Pb collisions at the LHC,” *Phys. Lett. B* **845** (2023) 138110, [arXiv:2211.15326](https://arxiv.org/abs/2211.15326) [nucl-ex].
- [58] K.-J. Sun *et al.*, “Suppression of light nuclei production in collisions of small systems at the Large Hadron Collider,” *Phys.Lett.B* **792** (2019) 132–137.
- [59] L. E. Marcucci, J. Dohet-Eraly, L. Girlanda, A. Gnech, A. Kievsky, and M. Viviani, “The hyperspherical harmonics method: A tool for testing and improving nuclear interaction models,” *Frontiers in Physics* **8** (2020) . <https://www.frontiersin.org/journals/physics/articles/10.3389/fphy.2020.00069>.
- [60] L. Contessi, N. Barnea, and A. Gal, “Resolving the  $\Lambda$  Hypernuclear Overbinding Problem in Pionless Effective Field Theory,” *Phys. Rev. Lett.* **121** no. 10, (2018) 102502, [arXiv:1805.04302](https://arxiv.org/abs/1805.04302) [nucl-th].